

Spectroscopic characteristics of synthetic olivine: An integrated multi-wavelength and multi-technique approach

M.D. DYAR,^{1,*} E.C. SKLUTE,¹ O.N. MENZIES,² P.A. BLAND,² D. LINDSLEY,³ T. GLOTCH,³
M.D. LANE,⁴ M.W. SCHAEFER,⁵ B. WOPENKA,⁶ R. KLIMA,⁷ J.L. BISHOP,⁸ T. HIROI,⁷ C. PIETERS,⁷
AND J. SUNSHINE⁹

¹Department of Astronomy, Mount Holyoke College, 50 College Street, South Hadley, Massachusetts 01075, U.S.A.

²Impacts and Astromaterials Research Centre, Department of Earth Science and Engineering, South Kensington Campus, Imperial College London, SW7 2AZ, U.K.

³Department of Geosciences, Stony Brook University, Stony Brook, New York 11794-2100, U.S.A.

⁴Planetary Science Institute, 1700 E. Fort Lowell, Suite 106, Tucson, Arizona 85719, U.S.A.

⁵Department of Geology and Geophysics, E-235 Howe-Russell, Baton Rouge, Louisiana 70803, U.S.A.

⁶Department of Earth and Planetary Sciences and McDonnell Center for the Space Sciences, Washington University, St. Louis, Missouri 63130-4899, U.S.A.

⁷Department of Geological Sciences, Brown University, Providence, Rhode Island 02912, U.S.A.

⁸SETI Institute/NASA-Ames Research Center, Mountain View, California 94043, U.S.A.

⁹Department of Astronomy, University of Maryland, College Park, Maryland 20742, U.S.A.

ABSTRACT

Spectroscopic measurements have been made of two suites of olivine minerals synthesized under slightly different conditions in 5–10 mol% increments across the solid solution from forsterite to fayalite. Here, we present Mössbauer results for the entire Fe-Mg olivine suite, as well as the results for only the fayalite end-member as an introduction to our team's other diverse spectral-analysis techniques and data that will be presented in forthcoming papers. Experimental methods used to synthesize both suites of samples are discussed here in detail, along with specifics of the analytical techniques used to study them. Electron microprobe data and Mössbauer spectra acquired at 293 K across the solid solution are presented first to characterize and address the presence of impurities in the broad suite of samples that may affect other spectroscopic methods. We then focus specifically on the fayalite end-member to illustrate its properties using multiple techniques. Fayalite is an especially important phase for different types of spectroscopy because, by definition, it contains an equal distribution of Fe²⁺ cations between the M1 and M2 octahedral sites. Thus, features associated with each of the two sites must represent equal numbers of Fe²⁺ cations, removing uncertainties associated with assumptions about order/disorder of Fe²⁺ and other cations. Mössbauer, Raman, thermal emission, attenuated total reflectance (ATR), specular reflectance, and visible to mid-infrared total reflectance studies are presented for fayalite. These include calculation of mid-infrared optical constants (n and k) and fundamental Mössbauer parameters: intrinsic isomer shift (δ_I), Mössbauer temperature (θ_M), and recoil-free fraction (f). Data from the different techniques are described and related, demonstrating the importance of multi-wavelength data to provide a complete characterization and understanding of the spectroscopic features in fayalite.

Keywords: Fayalite, olivine, Mössbauer, Raman, thermal emission, reflectance, visible region, infrared, optical constant, attenuated total reflectance

INTRODUCTION

Olivine and pyroxene are the dominant ferromagnesian mineral groups in most mafic igneous rocks that occur at the surface of the Earth. Olivine in particular is the dominant phase in the Earth's upper mantle, where the Fe-Mg species control many of the geophysical properties of the interior, such as heat transfer, electrical conductivity, and seismic wave velocities. Fe-Mg olivine also has a near-ubiquitous presence in extrusive igneous rocks as well as metamorphic rocks from granulite facies terranes.

The composition of olivine is an important parameter for interpretation of bulk-rock chemistry (as well as trace elements and oxygen isotopic data) from all types of terrestrial bodies. Forsterite/fayalite ratios can be used to evaluate conditions of reduction and oxidation (redox). Knowledge of the olivine composition within the rocks making up the surfaces of the terrestrial planets would have implications for understanding the redox conditions and the degree of weathering. These are important issues that can be constrained using different types of spectroscopy, largely through studies of naturally occurring olivines (e.g., Burns 1993; Sunshine et al. 2007). However, olivines composed solely of Fe²⁺ and Mg are rare in nature (though some

* E-mail: mdyar@mtholyoke.edu

occurrences are fairly close), because minor substitution of Mn^{2+} , Cr, Ca, Ni, Zn, and other cations is usually present. Such substitutions introduce ambiguity into conclusions that can be drawn about cation distribution between octahedral sites on the basis of spectroscopic evidence. Thus, careful spectroscopic characterizations (by multiple techniques) of end-member olivines from the pure forsterite (Mg_2SiO_4)-fayalite (Fe_2SiO_4) solid-solution series are important and needed to allow the mineral physics to be studied in an integrated manner and to enable more accurate interpretations of remote-sensing data.

To address these needs, we report here the first in a series of papers characterizing aspects of two suites of olivines synthesized under slightly different conditions in 5–10 mol% increments across the solid solution from forsterite to fayalite. The goal of this research effort is to identify, describe, and compare diagnostic spectroscopic features seen at various wavelengths and with different techniques and to directly relate these features to physical and compositional properties of olivine. This paper has three sections. First, experimental methods used to synthesize the entire suite of samples are discussed here in detail, along with specifics of the analytical techniques used to study them. Second, Mössbauer spectra acquired at 293 K across the solid solution are presented and discussed for the full compositional suite of olivine to characterize and address the presence of impurities in the broad suite of samples that may affect other spectroscopic methods to be presented in future papers. Third, results of Mössbauer, Raman, thermal emission, attenuated total reflectance (ATR), specular reflectance, and visible to mid-IR total reflectance studies, including calculation of its

mid-IR optical constants (n and k) and fundamental Mössbauer parameters: intrinsic isomer shift (δ), Mössbauer temperature (θ_M), and recoil-free fraction (f), are given for fayalite alone. Because fayalite contains, by definition, an equal distribution of Fe^{2+} cations between the two octahedral sites, M1 and M2, it is an especially important phase for different types of spectroscopy. The fact that site occupancy of Fe^{2+} between the two sites is constrained to be 1:1 by the lack of any other cations, such that features associated with each of the two sites must represent equal numbers of Fe^{2+} cations, removes uncertainties associated with assumptions about order/disorder of Fe^{2+} and other cations and spectral band assignments. Results from the different techniques are described and related, demonstrating the importance of multi-wavelength data to provide a complete characterization and understanding of the spectroscopic features in fayalite. In forthcoming manuscripts, we will explore detailed spectroscopic results of groups of these techniques across the entire olivine compositional range. Our eventual goal is to create a cross-correlated, multi-wavelength set of reference spectra for the Fe^{2+} -Mg olivine solid-solution series.

OLIVINE STRUCTURE

Because all of the spectroscopic techniques used in this study must be interpreted within the context of the crystal structure and chemistry of olivine, a brief review seems appropriate. Olivine is an orthosilicate with a general formula of M1M2SiO_4 , where both the M1 and M2 sites are 6-coordinated. Because Si^{4+} is nearly always stoichiometric, compositional variations occur in the two octahedral sites. The olivine structure (Fig. 1) is nearly

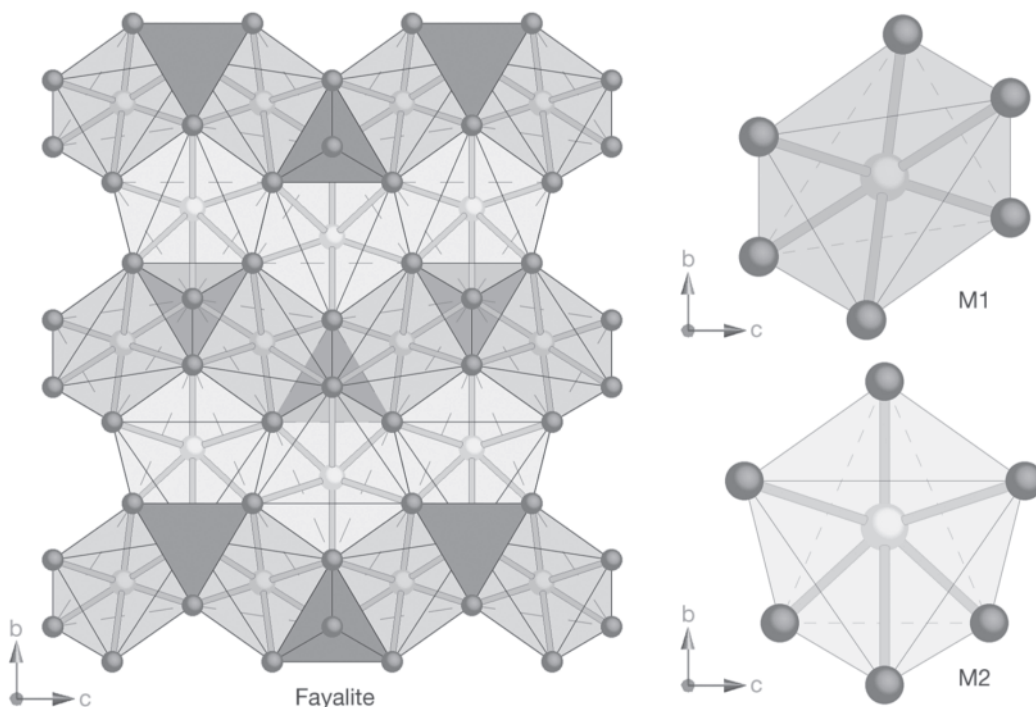


FIGURE 1. The crystal structure of fayalite, Fe_2SiO_4 . The isolated Si^{4+} tetrahedra are represented by the dark gray polyhedra, while the M1 and M2 Fe sites are shown as dark and light, respectively, distorted octahedra. The M1 and M2 octahedra form edge-sharing chains parallel to the c axis. In the M1 and M2 sites, the central Fe atom and its bonds to O are shown. On the right, the M1 and M2 octahedra have been isolated from the structure to show their different sizes and bond lengths.

hexagonally close-packed, with half of its octahedral interstices occupied by divalent cations, usually either Mg or Fe²⁺, and 1/8 of the tetrahedral sites occupied by Si⁴⁺. The nominally (Fe,Mg) O₆ octahedra share edges to create chains along the *c* axis; the chains have two alternating, distinct types of octahedra. The M1 site is slightly smaller and flattened along its threefold axis. The M2 site is slightly larger and is much more distorted; it generally contains the larger cations, such as Ca in monticellite. Divalent cations in olivine may be slightly ordered between the M1 and M2 sites. For example, both Ni²⁺ and Co²⁺ have a preference for the M1 sites based on their size and high octahedral site preference energies; this is observed from X-ray structure refinements as discussed in Bish (1981) and Ottonello et al. (1990), as well as in crystal field spectra (Hu et al. 1990). Mn²⁺, on the other hand, has no crystal field splitting energy, and thus its site occupancy is based on the best fit to its ionic radius, which is the M2 site in olivine (e.g., Burns 1970). More recent work has studied the effect of temperature on cation ordering in olivines (Henderson et al. 1996; Redfern et al. 2000). These studies suggest that Fe²⁺ shows a slight preference for M1 at temperatures <600 °C, but orders into M2 above that temperature. It is apparent that many factors, including ionic radius, octahedral site preference energies, crystal field splitting, vibration entropy, and changes in bond characteristics, influence cation ordering.

The ordering kinetics relevant to quenching of cation distributions in olivine have also been extensively studied (Aikawa et al. 1985; Akamatsu et al. 1993). These studies suggest that Mg-Fe cation distributions re-equilibrate very rapidly (with time scales of 10 ms), so that studies of quenched samples do not record high-temperature cation distributions. It is important to keep these conclusions in mind when drawing inferences about cation distributions based on meteoritic and other naturally occurring samples.

OLIVINE SYNTHESIS

Two different suites of samples were used in this study. The first suite (referred to here as “SUNY olivines”) was synthesized in the laboratory of Donald Lindsley at SUNY Stony Brook over a period of many years. These olivines were originally created for use as starting reactants in phase equilibria studies, but the samples were well suited to the current spectroscopic study. For a few missing compositions, additional material was needed to complete our suite of spectroscopic measurements, so a few samples were synthesized during the past year. The second set of samples, subsequently referred to as “Bristol olivines,” was synthesized by Richard Brooker in the Department of Earth Sciences, Bristol University, as part of a study relating the quadrupole splitting of olivine to its composition (Menzies et al. 2001).

At Stony Brook University, stoichiometric mixtures of SiO₂, MgO, and Fe₂O₃ were ground for 1–2 h under ethanol. An iron sponge was then added and grinding continued for <1 h. The product was wrapped in silver foil and placed in a silica-glass capsule. One end was sealed and the middle of the capsule was drawn out into a capillary, leaving the sample by the sealed end. An Fe getter was placed next to the open end of the capsule. The assembly was evacuated and then put into a vertical tube furnace at ~800 °C (the Fe getter remained at ~600 °C) for 10–20 min.

The capsule was taken out of the furnace and sealed across the capillary. The completely sealed capsule section containing the sample was then placed in a horizontal tube furnace at ~920–940 °C and cooked for 10 days. Samples were then quenched in water. Powders were removed and then examined by XRD to determine whether the olivine-producing reaction had gone to completion. In all cases, multiple “cycles” of drying/heating were needed to achieve complete reaction and produce olivines of the desired compositions. The SUNY samples were subsequently determined by Mössbauer spectroscopy to be completely reacted, resulting in 100% olivine (see Table 1 and discussion below).

At Bristol University, samples were prepared by the creation of stoichiometric mixtures of SiO₂, MgO, and Fe₂O₃ and grinding prior to pressing into pellets. Samples were crystallized at 1300 °C for forsterite end-members and 1100–1200 °C for samples with more than 50% Fe for three periods of 4 h each, with grinding and repelleting between heating episodes (Redfern et al. 2000). The experiments were buffered with a CO₂-CO gas mixture to be about one log unit more oxidizing than the Fe-FeO buffer. Pellets were quenched inside the furnace to below 500 °C in less than one minute. A single cycle of reduction/heating was used for each synthesis, resulting in impurities in the products that were first seen by Mössbauer studies (Table 1).

To characterize the impurities further, polished grain mounts of samples containing impurities were made, and careful electron microprobe analyses were undertaken at SUNY Stony Brook. Three Bristol samples, Fo₉₀, Fo₈₀, and Fo₆₀, were typical of samples in this suite. The Fo₉₀ samples are characterized by having a variable composition: forsterite contents ranged from 85–92. Many olivine grains had Ca-free pyroxene (probably orthopyroxene) cores. Ferropericlase with a composition near Per₈₀Wus₂₀ was also observed, along with several grains of nearly pure Fe oxide (probably hematite, magnetite, or wüstite). Roughly 1% of the grains had pure silica cores, Ca-free pyroxene inner rims, and olivine outer rims, suggesting that the starting materials were insufficiently ground to achieve complete reaction.

Fo₆₀ olivines from this suite had forsterite contents ranging from 53–64. We again observed a modest number of Si-rich cores, stoichiometric Ca-free pyroxene, and magnesiowüstite with good stoichiometry. Finally, the forsterite composition of the Fo₈₀ sample ranged from 78–82. Ca-free pyroxene and ferropericlase with good stoichiometry were also observed, suggesting that neither pyroxene nor oxide is the carrier of Fe³⁺ in these samples. Despite these impurities and the presence of Fe³⁺ as observed by Mössbauer, the Bristol olivines were included in this study as a potentially useful comparison suite to the “pure” synthetics that comprise the SUNY olivine suite.

SPECTROSCOPIC METHODS

Mössbauer

Approximately 4–24 mg of each sample were crushed under acetone, then mixed with a sugar-acetone solution designed to form sugar coatings around each grain and prevent preferred orientation. The amount of sample used was determined by the amount available. Grains were heaped gently in a sample holder confined by polyimide tape. Mössbauer spectra were acquired using a source of 100–40 mCi ⁵⁷Co in Rh on a WEB Research Co. model WT302 spectrometer (Mount Holyoke College) equipped with a scintillation detector. For the present study, we acquired spectra of all samples in both sample suites at 293 K to check for the presence of impurities and Fe³⁺. For pure fayalite, spectra also were acquired over a temperature

range from 4–293 K to determine the change in center shift and make it possible to calculate fundamental Mössbauer parameters, including intrinsic isomer shift, Mössbauer (Debye) temperature, and recoil-free fractions (f) for Fe^{2+} in the M1 and M2 sites. Many of our samples began to order magnetically at temperatures below 85 K; this ordering temperature is composition dependent (Sklute et al. 2006). Because combinations of states are extremely difficult to model, that work will be detailed in a separate publication. Thus, this study is restricted to the temperature range that produced useful data for assessing f . For fayalite (Fo_0), this range was 85–293 K.

For each sample, the fraction of the baseline due to the Compton scattering of 122 keV gammas by electrons inside the detector was determined by measuring the count rate with and without a 14.4 keV stop filter (~2 mm of Al foil) in the gamma beam. Compton-corrected absorption was calculated for each individual spectrum using the formulation $A/(1-b)$, where b is the Compton fraction and A is the uncorrected absorption, and ranged from 0.32–0.41 for these samples. This correction does not change the results of the fits per se, but does allow accurate determination of percentage of absorption in the spectra. It is necessary because the range of energy deposited in the detector by Compton events extends from 0 to 40 keV, overlapping the energies deposited by the 14 keV gammas. Further details on this procedure are found in Dyar et al. (2008).

Run times were 2–48 h, and baseline counts ranged from ~500 000 to 20 million after the Compton correction, as needed to obtain reasonable counting statistics. Spectra were collected in 2048 channels and corrected for nonlinearity via interpolation to a linear velocity scale, which is defined by the spectrum of the 25 μm Fe foil used for calibration. Data were then folded and summed before fitting, using a procedure that folds the spectrum about the channel value that produces the minimum least squares sum difference between the first half of the spectrum and the reflected second half of the spectrum.

To model the data, we used an in-house program generously made available to us by Eddy DeGrave and Toon VanAlboom at the University of Ghent, in Belgium, called MexfieldDD, which is well suited to modeling of highly overlapped spectra. MexfieldDD was used to provide Lorentzian line shapes and the capability of solving the full Hamiltonian. Quadrupole splittings (Δ), center shifts (δ , reference to $\alpha\text{-Fe}$), and linewidths (W) were generally allowed to vary freely, though some constraints on δ and Δ were used to model the very small doublets representing Fe^{3+} and other impurities. The Fe^{2+} peaks were arranged with the outermost doublets as a pair and the innermost doublets as a second pair. Areas were allowed to vary in pairs (e.g., the areas of peaks 1 and 4 were allowed to vary in unison, and the areas of peaks 2 and 3 were allowed to vary together). When impurities or Fe^{3+} were present, their areas were allowed to vary as doublet pairs as well.

Errors on center shifts and quadrupole splitting are estimated at better than

± 0.02 mm/s. The distribution of area between the two Fe^{2+} doublets is non-unique, and probably ± 5 –10% absolute, but the summed areas of the smaller (e.g., Fe^{3+}) components relative to the total area are accurate to within ± 1 –3% absolute.

To determine the fundamental Mössbauer parameters intrinsic isomer shift (δ), characteristic Mössbauer temperature (θ_M), and recoil-free fraction (f), we use the temperature dependence of the center shift (δ), described by the Debye integral approximation through the following relation (DeGrave et al. 1985):

$$\delta(T) = \delta_0 - \frac{9 k_B T}{2 M c} \left(\frac{T}{\theta_D} \right)^3 \int_0^{\theta_D/T} \frac{x^3}{e^x - 1} dx. \quad (1)$$

Here k_B is the Boltzmann constant, M is the mass of the ^{57}Fe nucleus, c is the speed of light, T is temperature, and θ_D is the Debye temperature of the absorber, which is equivalent to θ_M . The intrinsic isomer shift (δ_0) and characteristic Mössbauer temperature (θ_M) are parameters that arise from the Debye approximation for the lattice vibrations of an ideal crystal. The intrinsic isomer shift is the isomer shift that would exist in the absence of temperature-dependent lattice vibrations in the absorber (Lafleur and Goodman 1971), and the Mössbauer temperature is effectively the same as the Debye temperature of the solid.

To calculate f , Mössbauer spectra were acquired over a range of temperatures, from 4 K up to 300 K at 10–50° increments. Next, the Mössbauer temperature (an approximation of the Debye temperature, θ_D) and the center shift (δ) are calculated based on a fit of Equation 1 to the experimental data. Finally, the recoil-free fraction for each site is calculated using the approximation:

$$f(T) = \exp \left[-\frac{3 E_R}{2 k_B \theta_D} + \left[1 + 4 \left(\frac{T}{\theta_D} \right)^2 \int_0^{\theta_D/T} \frac{xdx}{e^x - 1} \right] \right] \quad (2)$$

where E_R is the recoil energy, related to the transition energy, E_γ by $E_R = E_\gamma^2/2Mc^2$.

The relationship between center shift and temperature was used to determine the characteristic Mössbauer temperatures θ_M of fayalite using a fit of the experimental data to Equation 1 above. Recoil-free fractions, f , were then estimated using Equation 2 above. This procedure was performed using both our own Mathematica routine and one written by E. DeGrave; both routines gave identical results. More information about the calculations can be found in DeGrave and VanAlboom (1991) and Eeckhout et al. (2003).

Recoil-free fraction information then can be used to estimate the relative Fe^{2+} occupancy of the two sites, using the formulation of Bancroft (1969):

TABLE 1. Analytical summary

Fo starting composition	Source	% Fe^{3+} @ 293 K	% Impure @ 293 K	MB 293	MB T series	Raman	RELAB VNIR	RELAB MIR	TES MIR	ATR	SPEC
0	SUNY	0.0	0.0	X	X	X	X	X	X	X	X
0	Bristol	2.1	17.4	X	X	X	X	X			
10	SUNY	0.0	0.0	X	X	X	X	X	X	X	X
10	Bristol	2.0	9.4	X	X	X	X	X			
20	SUNY	0.0	0.0	X	X	X	X	X	X	X	X
20	Bristol	3.7	<1.0	X	X	X	X	X			
30	SUNY	0.0	0.0	X	X	X	X	X	X	X	X
30	Bristol	3.2	0.0	X	X	X	X	X			
40	SUNY	1.2	0.0	X	X	X	X	X	X	X	X
40	Bristol	0.0	0.0	X	X	X	X	X			
50	SUNY	1.4	4.5	X	X	X	X	X	X	X	X
50	Bristol	<1.0	0.0	X	X	X	X	X			
60	SUNY	1.8	0.0	X	X	X	X	X	too small	X	X
60	Bristol	2.0	6.1	X	X	X	X	X			
70	SUNY	0.0	4.3	X	X	X	X	X	X	X	X
70	Bristol	1.2	0.0	X	X	X	X	X			
80	SUNY	2.7	0.0	X	X	X	X	X	X	X	X
80	Bristol	17.2	0.0	X	X	X	X	X			
89.5	SUNY	1.6	0.0	X	X	X	X	X	X	X	X
90	Bristol	9.4	18.7	X	X	X	X	X			
100	SUNY					X	X	X	X	X	X

Notes: Source is the originator/creator of the sample. % Fe^{3+} and % Impure (Fe^{3+} not in olivine) were derived from Mössbauer spectra. A listing of <1.0 means there is a feature just at the resolution of the technique that could not be fit. MB 293 indicates Mössbauer data collected at 293 K; MB T series are samples for which a suite of 16 Mössbauer spectra were collected at different temperatures from 4–293 K. Raman data were measured at WUSTL. RELAB VNIR data are bidirectional reflectance spectra measured in the RELAB 0.3 to 2.6 μm . RELAB MIR are off-axis biconical diffuse reflectance spectra measured in the RELAB 2 to 50 μm . TES MIR are thermal emission spectra measured at ASU from 5 to 50 μm . ATR are attenuated total reflection spectra measured at Caltech or SBU from 2.5 to 25 μm . SPEC are reflectance spectra measured at Caltech and/or SBU from 2.5 to 100 μm of prepared pellet samples.

$$\frac{A_{M1}}{A_{M2}} = C \frac{N_{M1}}{N_{M2}}, \quad (3)$$

where

$$C = \frac{\Gamma_{M1} G(X_{M1}) f_{M1}}{\Gamma_{M2} G(X_{M2}) f_{M2}}, \quad (4)$$

and C is a function of the ideal peak width Γ , sample saturation $G(x)$, and the Mössbauer recoil-free fraction f for each olivine site M1 and M2. The degree of correspondence between peak areas and actual Fe occupancy depends on three assumptions, namely that the linewidths of the peaks of each doublet are the same; saturation corrections are unnecessary if samples are correctly prepared as thin absorbers; and the recoil-free fraction for Fe^{2+} in both sites is the same. In this study, we kept peak widths (W) equivalent to satisfy the first assumption, and used thin absorbers to satisfy the second. So, the C correction factor is purely the ratio of the f values for M1 and M2, and the expression can be simplified to:

$$\frac{A_{M1} f_{M2}}{A_{M2} f_{M1}} = \frac{N_{M1}}{N_{M2}}. \quad (5)$$

Use of a pure fayalite end-member requires that N_{M1} and N_{M2} be equal, so the ratio of f_{M2}/f_{M1} can be calculated based on doublet areas alone. Thus, we have two methods for calculating the ratio of f_{M2}/f_{M1} based on the data set here: (1) use the temperature dependence of center shift and the Debye model, and (2) use the ratio of doublet areas in our fits and calculate the C value that corrects them to a 1:1 ratio.

Raman

Raman analysis was performed at Washington University with a fiber-optically coupled microprobe based on an axial spectrograph with volume holographic transmission gratings (HoloLab Series 5000 Raman Microscope from Kaiser Optical Systems, Inc.). The Raman microprobe technique does not require any sample preparation. A very small amount (a few pinhead-sized specs) of the fine-powdered sample is put on a regular glass slide placed on the stage of the instrument's research-grade microscope. The sample can be viewed in either reflected or transmitted light and individual micrometer-sized areas can be selected (and photo-documented, if necessary) for Raman analysis. Thus, in contrast to the other techniques used, Raman analysis does not provide an analysis of the bulk material, but rather, of individual spots.

The excitation light of 532 nm (18976 cm^{-1}) was delivered by a frequency-doubled Nd-YAG laser that was coupled into a Leica microscope (Leitz, Wetzlar, Germany) via an 8 μm single-mode optical fiber. An 80 \times ultra-long working distance objective (Olympus, Japan) with a numerical aperture of 0.75 and a working distance of 8 mm was used for focusing the light onto the sample, resulting in a lateral resolution of $\sim 1 \mu\text{m}$ and a power of less than 0.5 mW at the sample surface. The back-scattered light is collected through the same objective, focused onto the core of a 100 μm , multi-mode collection fiber, and guided into the spectrometer. The beam passes through a holographic element and splits into two parts that are then imaged onto a CCD array detector (Andor Technology) with 2048 channels (upper pixels image 100–2500 Δcm^{-1} , whereas the lower pixels image 2500–4400 Δcm^{-1}) and a spectral resolution of 2.5 cm^{-1} . Thus, the whole spectral range of interest in Raman spectroscopy from 100–4200 Δcm^{-1} (corresponding to 534 to 685 nm) can be detected simultaneously.

Spectra were acquired with the Holograms software (Kaiser Optical Systems, Inc.), and spectral acquisition time per 1 μm analysis spot was 256 s. Ten different spots were analyzed in each of the Fo_0 samples. Spectral processing was performed with the Grams/32 Software (Galactic Industries from Thermo Scientific).

RELAB bidirectional and biconical reflectance

Visible and near-infrared (VNIR) spectra were acquired using the bidirectional reflectance (BDR) spectrometer at the NASA/Keck Reflectance Experiment Laboratory (RELAB) at Brown University. Spectra of both $<45 \mu\text{m}$ grain-size fraction powders were measured relative to a halon reference standard at 5 nm resolution over the wavelength range of 0.3–2.6 μm and corrected for the small features of halon. An incidence angle of 30° and an emission angle of 0° were selected for bidirectional measurements. After the SUNY sample was prepared as a pressed pellet (see ATR and specular reflectance section below), it was re-measured under the same geometric conditions.

Diffuse biconical reflectance spectra were also collected for the same powders and pellet in a purged (CO_2 - and H_2O -free) environment using a Pike diffuse reflectance accessory fitted to a Thermo-Nicolet Nexus 870 Fourier transform infrared (FTIR) spectrometer with an off-axis biconical viewing geometry. Spectra were collected at 4 cm^{-1} resolution and 2 cm^{-1} intervals using a deuterated triglycine sulfate (DTGS) detector and either a KBr beamsplitter (from 1.3–25 μm ; ~ 400 –7700 cm^{-1}) or a solid substrate beamsplitter (particulates measured from 16–50 μm ; 200–625 cm^{-1} , pellet measured from 16–100 μm ; 100–625 cm^{-1}). Raw spectra were rationed to a diffuse gold reference standard and then scaled to the bidirectional spectra near 2.5 μm to provide absolute reflectance values.

VNIR spectral modeling

VNIR BDR spectra were modeled using the Modified Gaussian Model (MGM). The MGM uses a stochastic inversion to deconvolve a spectrum into a continuum and a series of modified Gaussian curves that can be attributed to specific electronic absorptions (Sunshine et al. 1990; Sunshine and Pieters 1998). A preliminary fit to the fayalite sample was performed using six bands: three spin-allowed crystal field bands to model the complex absorption near 1 μm , and three broad bands in the VNIR. These bands were superimposed on a continuum that was allowed to slope linearly in wavelength space. The model was allowed to iterate until the change in RMS error was less than 1E-5.

The results of the initial six-band model were input as starting parameters for a more comprehensive model solution that also includes bands for the weak spin-forbidden crystal field absorptions using the approach of Klima et al. (2007). Spin-forbidden absorptions are one or more orders of magnitude weaker than spin-allowed crystal field bands. Thus, for this fit, the model was allowed to iterate until the change in RMS error was less than 1E-7. Ten spin-forbidden transitions are predicted to occur between 300–550 nm when Fe^{2+} resides in olivine (5 each for the M1 and M2 sites). These bands are superimposed on stronger charge-transfer absorptions, and may not all be clearly discernable in a reflectance spectrum. Two approaches were used to isolate the number and positions of spin-forbidden bands necessary to model the spectrum. For the first approach, the spectrum and RMS error by wavelength for the preliminary six-band fit were inspected visually to determine where additional bands were needed. For the second approach, 10 bands were added at the approximate wavelengths predicted for the M1 and M2 sites using a Tanabe-Sugano energy level diagram for Fe^{2+} in octahedral coordination. In both cases, the model was run with the bands in the 1 μm region held fixed. This is necessary to ensure that the large number of bands added in the VNIR do not cause the model to arrive at a mathematically accurate but physically unrealistic solution.

ATR and specular reflectance

Attenuated total reflectance (ATR) and specular reflectance spectra were acquired at Stony Brook University on a Nicolet 6700 FTIR spectrometer purged of CO_2 and H_2O . ATR spectra of the SUNY fayalite loose powder (Fo_0 SUNY) were acquired from 400–4000 cm^{-1} using a SmartOrbit ATR attachment with a type IIA diamond ATR element. For these measurements, the FTIR was equipped with an uncooled DLATGS detector with a KBr window and a KBr beamsplitter. Spectra were collected at 4 cm^{-1} resolution.

The SUNY olivine samples were then pressed into 5 mm diameter compact disks (pellets) using a Carver hydraulic press and a KBr pellet press and die. The pressing process produces a flat surface for which single specular reflections can be assumed in the mid- and far-IR spectral ranges (e.g., Roush et al. 1991; Glotch et al. 2004). At wavenumbers greater than $\sim 2000 \text{cm}^{-1}$ the assumption of a single specular reflection with no scattering becomes less and less valid, so spectral analyses of pressed pellets are generally confined to the $<2000 \text{cm}^{-1}$ region.

Specular reflectance spectra (100–4000 cm^{-1}) of the Fo_0 SUNY pellet (Fo_0 SUNY-P) were acquired using a FT-30 specular reflectance accessory with incidence and reflection angles of 30°. These spectra were acquired in two parts—4000–400 cm^{-1} using the same beamsplitter and detector as the ATR spectra; and 600–100 cm^{-1} using a Nicolet Solid Substrate beamsplitter and a DTGS detector with a polyethylene window. Several corrections were applied to the spectra to make them optimal for dispersion modeling. First, we characterized the “reflectance function” of the reflectance accessory and standard by acquiring a background spectrum without the accessory in the spectrometer. The accessory was then inserted into the spectrometer with the reflectance standard, and a spectrum was collected. This spectrum represents the combined reflectance of the mirrors in the reflectance accessory and the reflectance standard. Because the olivine pellets are small compared to the size of the incident beam, we accounted for the reflectance properties of the aperture mask upon which the pellets sit. The bottom of the mask was coated with black paraffin wax soot to reduce the reflectance of

the mask as much as possible. Subsequent to the collection of the olivine pellet spectra, we acquired a spectrum of the “blank” aperture mask to characterize its reflectance. Both the olivine pellet and blank spectra were divided by the response function spectrum. The blank spectrum was then subtracted from the pellet spectra. Mid- and far-IR spectra were merged near 500 cm^{-1} to produce a single spectrum covering the range from $100\text{--}2000\text{ cm}^{-1}$.

We used the reflectance spectrum of the Fo_0 pellet to determine the bulk real and imaginary indices of refraction (optical constants) of fayalite. Two additional corrections were applied to the reflectance spectrum to ensure that the derived optical constants are as accurate as possible. Ideally, optical constants are derived from reflectance spectra of single crystals. Comparison of the Fo_0 pellet spectrum to single-crystal fayalite reflectance spectra of Suto et al. (2002) indicates that the maximum reflectance of the pellet is significantly less than that of a polished single crystal. Therefore, we multiplicatively scaled the spectral contrast of the pellet spectrum to match that of the single-crystal spectra. In addition, the portion of the spectrum shortward of the Christiansen frequency (1026 cm^{-1}) has a significantly higher reflectance than that of the single-crystal spectra. This may be due to increased multiple scattering of the pellet at shorter wavelength regions. Therefore, we multiplied the portion of the spectrum shortward of the Christiansen frequency by a factor of 0.66 to match the single-crystal spectra. All of these corrections were necessary to correctly determine the bulk optical constants of fayalite. To determine the optical constants, we made use of the dispersion equations defined by Spitzer and Kleinman (1961). Spectra were modeled as a series of coupled Lorentzian oscillators defined by three parameters: ν , the center frequency of the oscillator, $4\pi\mu$, the oscillator strength, and γ , the damping coefficient. A fourth parameter ϵ_0 , the high-frequency dielectric constant is unique to each mineral, and should be equal to n_{vis}^2 (Roush et al. 1991). Oscillator parameters were entered into a dispersion model and iteratively refined using a nonlinear least-squares fitting algorithm described by Glotch et al. (2007).

Mid-infrared thermal emission

Thermal emission data were acquired at the Arizona State University (ASU) Mars Space Flight Facility. The ASU lab hosts a Nicolet Nexus 670 FTIR spectrometer that has been modified for emission measurements by removal of the SiC source and placement of an enclosed glovebox and folding mirrors outside the spectrometer housing that enable the energy from a heated sample in an external sample chamber to enter into the ray path for measurement. The wall of the sample chamber is water-cooled to maintain the environmental temperature. The atmosphere is purged of CO_2 and H_2O to eliminate their spectral lines from the sample data. The spectrometer is equipped with a thermoelectrically stabilized DTGS detector and a CsI beamsplitter that allows quality measurement of emitted radiation over the mid-infrared range of ~ 2000 to 240 cm^{-1} . For measurement, the olivine Fo_0 sample pellet was placed in a copper sample cup painted with Aeroglaze Z302 gloss black paint, and heated to and maintained at a 350 K set-point for the duration of the measurements. The 160 scans of the sample were acquired at 4 cm^{-1} spectral resolution (2 cm^{-1} intervals) and the individual-scan spectra were averaged together. This sample radiance spectrum was calibrated according to the procedure discussed in detail in Ruff et al. (1997) and converted to spectral emissivity. Because the sample was very small ($< 5\text{ mm}$ diameter) and the spot size measured by the spectrometer ($> \sim 1\text{ cm}$ diameter) is larger than the sample, it was necessary to subtract a large fraction ($\sim 90\%$) of the emissivity spectrum of an empty sample cup (a blank) from the calibrated sample emissivity spectrum to return a representative mineral spectrum.

RESULTS

Mössbauer

Mössbauer spectra of samples from both the SUNY and Bristol olivine suites are shown in Figures 2 and 3, respectively. The spectra of the Bristol olivine suite contain several smaller features at energies ranging from $0.3\text{--}1.5\text{ mm/s}$. Fits to some of these spectra are given in Figure 4, and Mössbauer data for all synthetic olivines at 293 K are given in Table 2.

Three different populations of doublets other than those assigned to Fe^{2+} in olivine were apparent in spectra of the Bristol series samples. (1) Several samples contained a poorly resolved Fe^{3+} doublet with parameters of $\delta = \sim 0.1\text{ mm/s}$ and $\Delta = \sim 0.45\text{ mm/s}$. EMPA results with good stoichiometries (as discussed

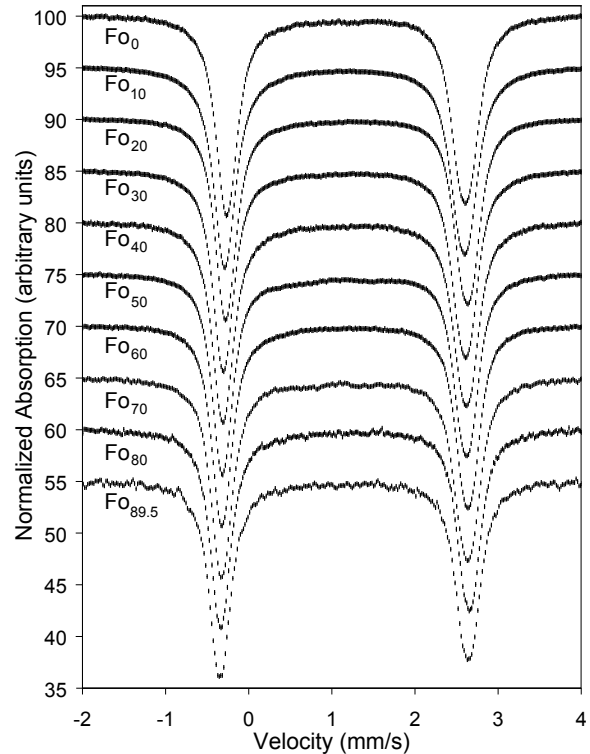


FIGURE 2. 293 K Mössbauer spectra of synthetic olivines (SUNY suite) synthesized in the laboratory of Donald Lindsley at SUNY Stony Brook. For the purposes of this comparison, all spectra have been scaled to the same percentage of absorption as the $\text{Fo}_{89.5}$ spectrum.

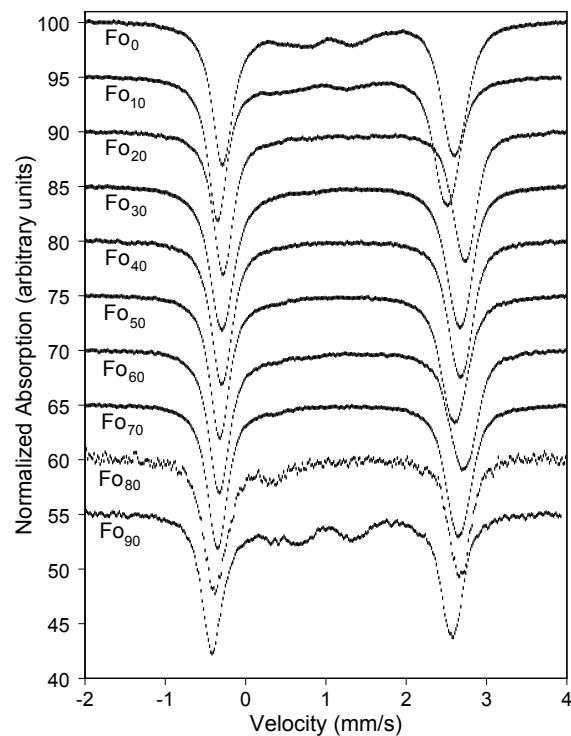


FIGURE 3. 293 K Mössbauer spectra of synthetic olivines (Bristol suite) synthesized at Bristol University. For the purposes of this comparison, all spectra have been scaled to the same percentage of absorption as the Fo_{90} spectrum.

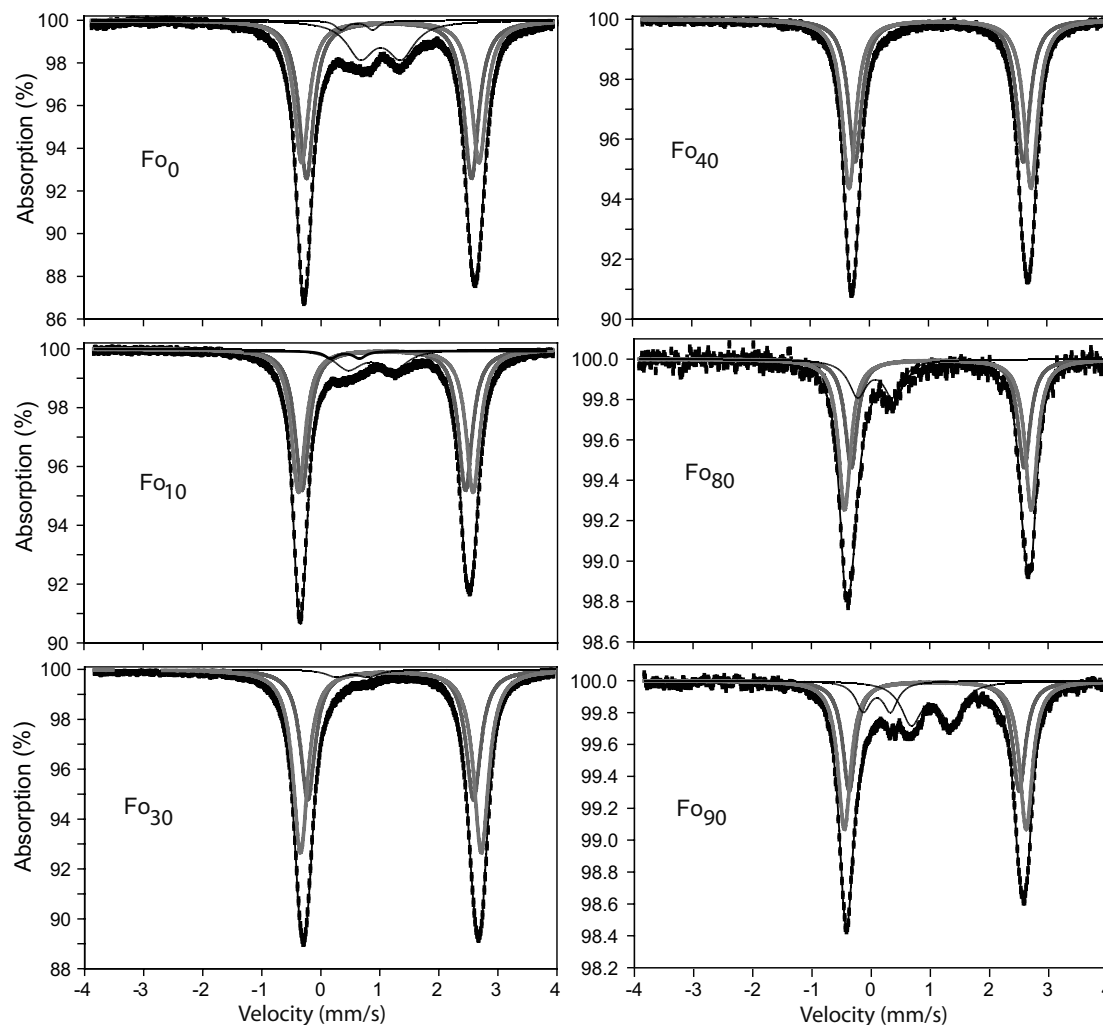


FIGURE 4. Fits to 293 K olivine spectra (Bristol suite) synthesized at the University of Bristol (Fig. 2), showing impurities and Fe^{3+} .

above) argue against the Fe^{3+} being present in the Ca-free pyroxene or ferropericlasite. Experimental control of oxygen fugacity suggests that olivine is unlikely to be accommodating Fe^{3+} . Thus, we hypothesize that the Fe^{3+} represented by these doublets is hosted in some type of probably nanophase Fe oxide, but it is too poorly resolved to allow a specific assignment to any mineral. (2) In other samples, a Fe^{3+} doublet with $\delta = 0.4\text{--}0.6$ mm/s and $\Delta = 0.11\text{--}0.53$ mm/s was resolved, but it is also too highly overlapped with the dominant Fe^{2+} to be assigned to any specific phase. (3) Several other Bristol samples also contained conspicuous Fe^{2+} doublets with $\delta = \sim 1.0$ mm/s. These features are probably due to un-reacted oxide such as ferropericlasite. The Bristol Fo_0 sample contains notably high percentages of these impurities: $\sim 2\%$ of the total Fe is present as nanophase hematite, and $\sim 17\%$ of the total Fe is present in oxide, probably wüstite on the basis of phase equilibria and the EMPA results noted above.

It is apparent from inspection of Figure 2 that the SUNY olivine spectra are composed of only two well-defined peaks, as expected from completely reacted syntheses under controlled oxygen fugacity. For this reason, the SUNY olivines are generally most representative of the spectral characteristics of true Mg- Fe^{2+} solid-solution compositions, although several of the

Bristol intermediate Fo samples are also of high purity (see Table 1). Data from the independently synthesized Bristol suite are included in this study to confirm and support the trends observed in the SUNY suite.

Mössbauer parameters for two-doublet fits to the temperature series data for the SUNY end-member fayalite are given in Table 3 and shown graphically in Figure 5. As expected, δ changes smoothly with temperature. As a result, the f values calculated on the basis of δ also follow smooth trends, although the f values for each doublet are distinctive. These plots do not allow M1 and M2 to be distinguished. However, the data in Table 3 do provide a good data set for estimation of the fundamental Mössbauer parameters θ_M and f of fayalite. The only analogous determinations that exist in the literature are $\theta_M = 380$ K and $f_{293} = 0.74$ for an olivine with unknown composition (DeGrave and VanAlboom 1991). Unfortunately, that study used only one-doublet fits, so the results cannot be directly compared to those of the current work. However, those parameters do fall between those for the two doublets in this study (Fig. 5).

The quadrupole splittings determined from the spectra are also very systematic (Fig. 5), but the areas of the two doublets, which should be constant at all temperatures, are not. Between 80

TABLE 2. Mössbauer results for 293 K spectra of synthetic olivines*

Composition	Fo ₀	Fo ₁₀	Fo ₂₀	Fo ₃₀	Fo ₄₀	Fo ₅₀	Fo ₆₀	Fo ₇₀	Fo ₈₀	Fo ₋₉₀
SUNY										
δ (mm/s)	1.16	1.14	1.17	1.14	1.14	1.14	1.15	1.14	1.14	1.14
Δ (mm/s)	2.76	2.79	2.80	2.80	2.81	2.82	2.85	2.85	2.88	2.89
Γ (mm/s)	0.29	0.32	0.27	0.28	0.29	0.27	0.27	0.28	0.27	0.27
%Area	48.4	44.2	46.3	45.2	41.6	45.0	45.4	44.7	44.5	44.4
δ (mm/s)	1.18	1.17	1.19	1.16	1.16	1.16	1.17	1.16	1.17	1.16
Δ (mm/s)	2.96	2.95	3.01	3.00	3.00	3.02	3.04	3.04	3.08	3.07
Γ (mm/s)	0.29	0.32	0.27	0.28	0.29	0.27	0.27	0.28	0.27	0.27
%Area	51.6	55.8	53.7	54.8	58.4	55.0	54.6	55.3	55.5	55.6
χ ²	6.32	9.65	6.98	6.29	1.55	14.3	1.85	2.76	1.56	1.03
Bristol										
δ (mm/s)	1.15	1.07	1.21	1.18	1.18	1.12	1.17	1.15	1.14	1.07
Δ (mm/s)	2.79	2.76	2.88	2.81	2.84	2.83	2.91	2.89	2.92	2.87
W (mm/s)	0.30	0.28	0.26	0.30	0.27	0.29	0.29	0.28	0.25	0.26
%Area	42.4	43.8	40.7	40.2	45.8	51.5	41.8	50.8	34.7	30.6
δ (mm/s)	1.17	1.10	1.23	1.19	1.20	1.16	1.21	1.17	1.14	1.08
Δ (mm/s)	3.00	2.95	3.10	3.06	3.07	3.03	3.14	3.11	3.15	3.07
W (mm/s)	0.30	0.28	0.26	0.30	0.27	0.29	0.29	0.28	0.25	0.26
%Area	38.2	44.8	55.5	56.6	54.2	48.5	50.0	48.0	48.1	41.3
δ (mm/s)	0.61	0.50	0.10	0.54			0.10	0.40	0.08	0.10
Δ (mm/s)	0.53	0.49	0.45	0.54			0.45	0.11	0.59	0.46
W (mm/s)	0.24	0.25	0.40	0.44			0.30	0.19	0.38	0.30
%Area	2.1	2.0	3.7	3.2			2.0	1.2	17.2	9.4
δ (mm/s)	1.01	0.88					0.98			1.01
Δ (mm/s)	0.69	0.78					0.85			0.67
W (mm/s)	0.55	0.47					0.84			0.42
%Area	17.4	9.4					6.1			18.7
χ ²	8.27	4.30	3.46	3.95	2.57	5.69	2.06	3.94	0.78	7.74

* For this table, data were rounded to two digits after the decimal for δ, Δ, and W, and one digit after the decimal for %Area to reflect known error bars (±0.02 mm/s for δ, Δ, and W, and ±5% for area). The first two groups of data for both sets of samples are features assigned to Fe²⁺ in olivine. The third set of Bristol data represents doublets assigned to Fe³⁺ in an unknown phase, while the fourth set represents iron in an unreacted oxide such as ferroperricite. See text for details.

TABLE 3. Mössbauer temperature series for SUNY fayalite

Temperature	293	275	250	225	200	175	150	125	100	90	85
δ (mm/s)	1.16	1.18	1.20	1.22	1.24	1.25	1.27	1.28	1.29	1.30	1.30
Δ (mm/s)	2.76	2.80	2.85	2.89	2.92	2.93	2.96	2.97	2.98	2.98	2.99
W (mm/s)	0.29	0.29	0.29	0.29	0.30	0.29	0.29	0.29	0.29	0.30	0.30
%Area	48.4	48.4	48.4	48.4	48.4	48.4	48.4	48.4	48.4	48.4	48.4
δ (mm/s)	1.18	1.19	1.20	1.22	1.23	1.25	1.26	1.27	1.28	1.29	1.29
Δ (mm/s)	2.96	2.99	3.02	3.05	3.09	3.12	3.15	3.17	3.18	3.20	3.20
W (mm/s)	0.29	0.29	0.29	0.29	0.29	0.29	0.29	0.29	0.29	0.29	0.29
%Area	51.6	54.0	54.0	53.2	53.3	53.8	50.4	51.4	51.2	51.8	51.7
χ ²	6.32	6.62	4.38	3.71	10.59	5.23	9.16	10.45	38.00	3.23	3.57

Note: For this table, data were rounded to two digits after the decimal for δ, Δ, and W, and one digit after the decimal for %Area to reflect known error bars, which are given in Table 2.

and 150 K, the curves for each doublet appear to follow sloping curves, but above 175 K, the doublet areas are roughly constant (especially with the ca. 5% absolute error bars). These data suggest that the peak areas overlap too much to be meaningful, and this will, in turn, impact values for *C* (the correction factor) that are calculated on the basis of areas alone.

This comparison is shown in Figure 6, where values of *C* based on the Debye model calculations (“theoretical”) are compared with the calculated *C* values based on doublet areas (“experimental”). Because the curves in Figure 5 for the changes in center shift and *f* with temperature are gradual and systematic, the resultant theoretical *C* values, which are simply the ratio of the bigger *f* value over the smaller one, are also systematic. However, the experimental determinations for *C* give apparently random results. It is intriguing that doublets in the olivine spectra that are too poorly resolved to give meaningful areas still define consistent trends in δ, sufficient to define δ_i, θ_M, and *f* so well.

It is also possible that the Debye model used to calculate the theoretical *f* values is not robust, though previous workers have found this technique to yield useful information in past studies

(DeGrave and Van Alboom 1991; Eeckhout and DeGrave 2003). Finally, it is possible that there are vacancies that change the true site occupancy of Fe²⁺ to be something other than 1:1, thus violating the simplifying assumption made in the calculations based on Equation 5 (namely, that $N_{M1} = N_{M2}$).

Raman

The Raman spectrum of fayalite is typical of olivine in that it shows both the so-called “internal” modes of the SiO₄ tetrahedra above 300 Δcm⁻¹, and the “external” or lattice modes below 300 Δcm⁻¹ (81 optical modes are theoretically possible; for detailed peak assignments see Chopelas 1991). The strongest and most characteristic Raman peaks in olivines are at ~820 and ~850 Δcm⁻¹, called the “olivine doublet.” The positions of these Raman bands are independent of crystal orientation and are correlated only with the chemical composition of the olivines. The wavenumber positions of those two peaks are inversely correlated with Fe concentration. The relative wavenumber positions of both peaks in the “olivine doublet” show monotonic shifts as a function of cation substitution between forsterite and fayalite,

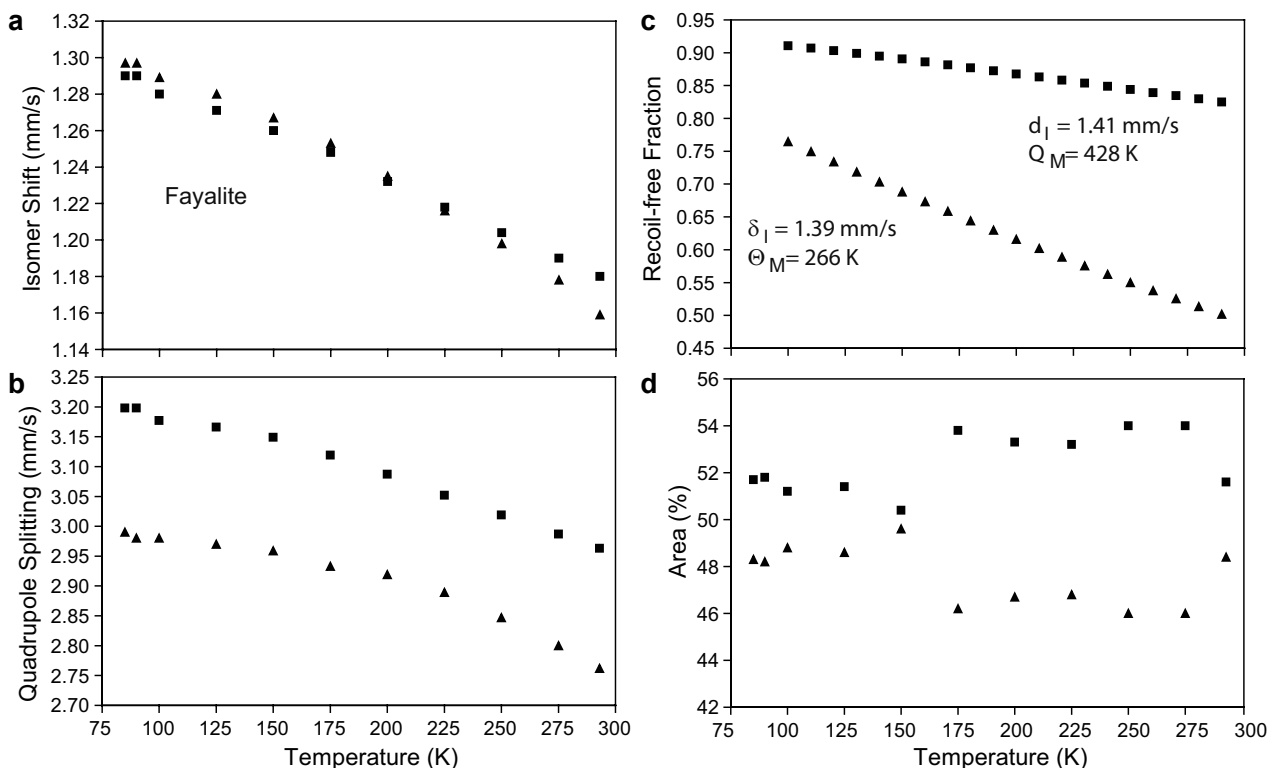


FIGURE 5. Temperature dependence of isomer shift (a), quadrupole splitting (b), and area (d) of Fe^{2+} olivine doublets in the Mössbauer spectra of fayalite (SUNY suite), along with calculated values for f (recoil-free fraction, c). Squares represent parameters calculated on the basis of pairing peaks 1 and 4 in the spectra, which triangles represent parameters resulting from pairing peaks 2 and 3. Data are plotted with three digits of precision after the decimal (even though known errors are ± 0.02 mm/s) to more clearly show subtle differences between data points.

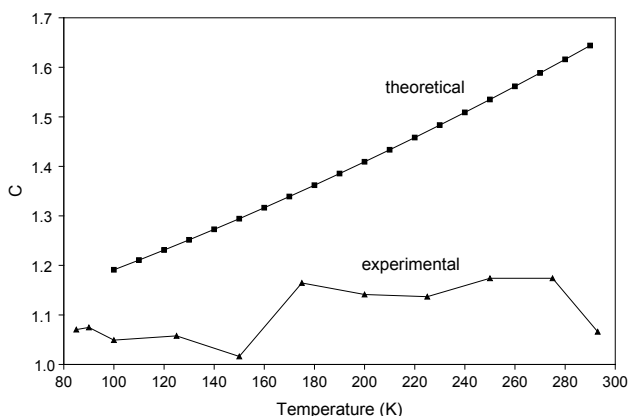


FIGURE 6. Comparison of C (correction factor) values for olivine showing experimental values based on area ratios and theoretical values of C vs. temperature (derived with help of Eq. 4). The lack of agreement between these two lines suggests three possibilities: (1) the two doublets corresponding to M1 and M2 are too highly overlapped to yield reliable area ratios; (2) the Debye model (Eqs. 1 and 2) used to calculate the f values is not robust; and (3) there are cation vacancies and/or Fe^{3+} present that change the true site occupancy of Fe^{2+} to be something other than 1:1, thus violating the simplifying assumption made in the experimental calculations.

and therefore can be used to derive the Fo-Fa composition of olivines (Kuebler et al. 2006).

Compared to the Raman spectra of Mg-containing olivines,

however, the spectrum of Fo₀ SUNY (Fig. 7, bottom) is unusual in several aspects. First, the positions of the two peaks of the olivine doublet (a combination of ν_1 symmetric and ν_3 asymmetric stretching modes) are extremely low, i.e., at 811 and 839 Δcm^{-1} . Second, additional peaks on the right hand side of the olivine doublet (e.g., at 899 Δcm^{-1}) are very poorly resolved or not resolved at all. Third, the peaks at low wavenumbers, especially the ones at 216 and 284 Δcm^{-1} , are unusually strong relative to the internal SiO_4 modes at higher wavenumbers. Fourth, the symmetric bending mode ν_2 at ~ 393 Δcm^{-1} and the asymmetric bending modes ν_4 at ~ 503 and ~ 568 Δcm^{-1} are very broad, with an additional, unexpected peak at ~ 591 Δcm^{-1} . Fifth, the broad peak at ~ 1300 Δcm^{-1} is caused by an artifact or contamination.

Actually, the spectrum of the Fo₀ SUNY sample at the bottom of Figure 7 shows the peaks for two minerals. The peaks at 151, 168, ~ 393 , ~ 503 , ~ 568 , 811, 839, and 899 Δcm^{-1} are caused by fayalite. The peaks at ~ 393 , ~ 503 , and ~ 568 Δcm^{-1} are caused by overlaps of the peaks for both fayalite and hematite, whereas the peaks at 216, ~ 591 , and ~ 1300 Δcm^{-1} are exclusively caused by hematite (synthetic hematite has strong Raman peaks at 219 and 284 Δcm^{-1} and weak Raman peaks at ~ 400 , ~ 488 and ~ 599 Δcm^{-1} ; see Martin et al. 1977). In the case of 532 nm excitation, an additional broad band at ~ 1300 Δcm^{-1} is present for hematite that is caused by the uncommon effect of “resonant two-magnon scattering” (Martin et al. 1977). Although the fayalite peaks were always the dominant features in the spectra of every grain studied from the SUNY Fo₀ sample, no grains had clean spectra of olivine

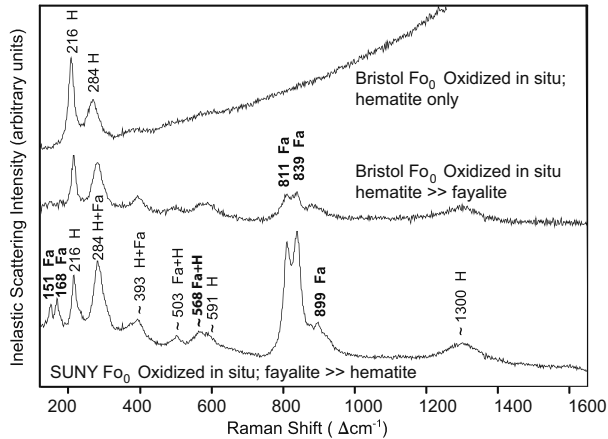


FIGURE 7. Raman spectra of Fo_0 Bristol (top two spectra) and Fo_0 SUNY (bottom spectrum). The diagnostic strong “olivine doublet” was found to be at 811 and 839 Δcm^{-1} for fayalite Fo_0 , but peaks for hematite were also present in the SUNY sample. These measurements, which resulted in a change in mineralogy, were made on separate splits of the synthetic samples; thus, these aliquots were not subsequently analyzed by the other techniques.

peaks only. The detected hematite was most likely created via in situ oxidation while the analyzed micrometer-sized sample spot was being irradiated by the laser.

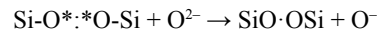
Raman spectra were also measured on micrometer-sized spots on grains separated from the Bristol Fo_0 sample (Fig. 7), but again no spots that showed pure olivine spectra could be found due to the impurity and/or instability of the sample. All analyzed locations showed characteristic hematite spectra, and it was apparent that hematite was being created almost instantaneously (i.e., during the first 1–2 s of data acquisition) due to heating by the laser beam. In fact, it was almost impossible to detect olivine peaks in most grains of this sample; in a few grains, only very weak olivine features were observed (Fig. 7, middle spectrum). Some spots in the Bristol Fo_0 sample also showed the presence of organic C-H bands $\sim 2900 \Delta\text{cm}^{-1}$ (not shown in Fig. 7). Typical spectra are shown at the top of Figure 7.

Because Fe^{3+} was not detected with any of the other analytical techniques that were used to characterize other (different) aliquots of this sample, we conclude that the fayalite was oxidized in situ under the laser beam during Raman analysis, despite the fact that the laser power was chosen to be extremely low. The oxidation to hematite occurred much faster and/or was much more likely in the Bristol Fo_0 sample compared to the SUNY Fo_0 sample.

The same phenomenon of oxidation to hematite is seen in Raman measurements of goethite and magnetite and other iron oxides and iron hydrates, especially if high laser power density is used for the excitation (e.g., de Faria et al. 2007). From the Raman spectroscopic perspective and the results obtained on both the SUNY and Bristol fayalites, Fo_0 has to be considered a very “labile” mineral. However, the good news for extraterrestrial research is that such oxidation is unlikely in a planetary environment where atmospheric oxygen content is nearly negligible. Furthermore, end-member fayalite is quite unusual in natural occurrences; even the smallest amount of Mg in the

olivine makes the sample stable so that this oxidation does not occur, even in terrestrial laboratories.

The dark color of Fe-rich phases causes them to be particularly subject to laser-induced heating. The instability that we recorded in our Fo_0 spectra may be due to the electronic states associated with O^- in the olivine structure, as described by Teichgraber and Freund (2008). They have observed changes in Raman peaks even in light-colored end-member Fo_{100} measured up to 673 K. At room temperature, two O^- are tightly coupled and inactive in the form of peroxy links, Si-OO-Si. Upon heating the peroxy link breaks up and an electron from a neighboring O^{2-} substitutes in:



where the dot represents an electron trapped in the now broken peroxy bond, while the neighboring O^{2-} has become an O^- . This hole is highly mobile (by a phonon-assisted electron hopping mechanism) and can travel at speeds on the order of 200 m/s.

In summary, based on the peak positions of the olivine doublet, the Raman measurements have confirmed that the SUNY samples are pure fayalite (Fo_0) and that it is a very labile phase. For the purposes of our integrated study, the fact that the Raman measurements have apparently partially oxidized the sample means that we will be unable to integrate the Raman data across techniques for the Fo_0 sample. It is also important to note that the Raman measurements were made on very small, 1–3 mg aliquots given to Washington University. Thus, the Raman measurements were made on a completely different split of these samples than the other measurements, and the data in no way imply that hematite should be present in the other splits.

Diffuse reflectance

Bidirectional and biconical reflectance spectra of the synthetic fayalites Fo_0 Bristol and Fo_0 SUNY are presented in Figure 8. Both samples were measured as fine-grained particulate samples. In addition, the pressed pellet form for SUNY Fo_0 (Fo_0 SUNY-P) was also measured. The VNIR spectra of all samples (Fig. 8a) are dominated by a complex absorption near 1 μm (1000 nm). This feature is a composite of three spin-allowed crystal field absorptions: two caused by Fe^{2+} in the M1 site and one caused by Fe^{2+} in the M2 site of olivine (e.g., Burns 1993). For Fo_0 SUNY, the overall shape of the 1000 nm feature is consistent with that measured previously for natural fayalite (Sunshine and Pieters 1998). The spectrum of Fo_0 Bristol is significantly darker with less spectral contrast across the visible than the Fo_0 SUNY spectrum, suggesting contamination by an opaque material in Fo_0 Bristol. An additional feature, not diagnostic of olivine, is present near 550 nm (open arrow, Figs. 8a and 8c), also suggesting contamination by another phase. The spectrum of the Fo_0 SUNY-pellet is broadly similar to the spectrum of Fo_0 SUNY, though with substantially reduced spectral contrast throughout due to a shorter average path length. The compressed nature of the pellet restricts the amount of light allowed to pass into particles of the sample and subsequently less is scattered out.

Radiation must penetrate into the crystal structure of a silicate mineral and be reflected out via multiple scattering events to detect absorptions throughout the VNIR, including

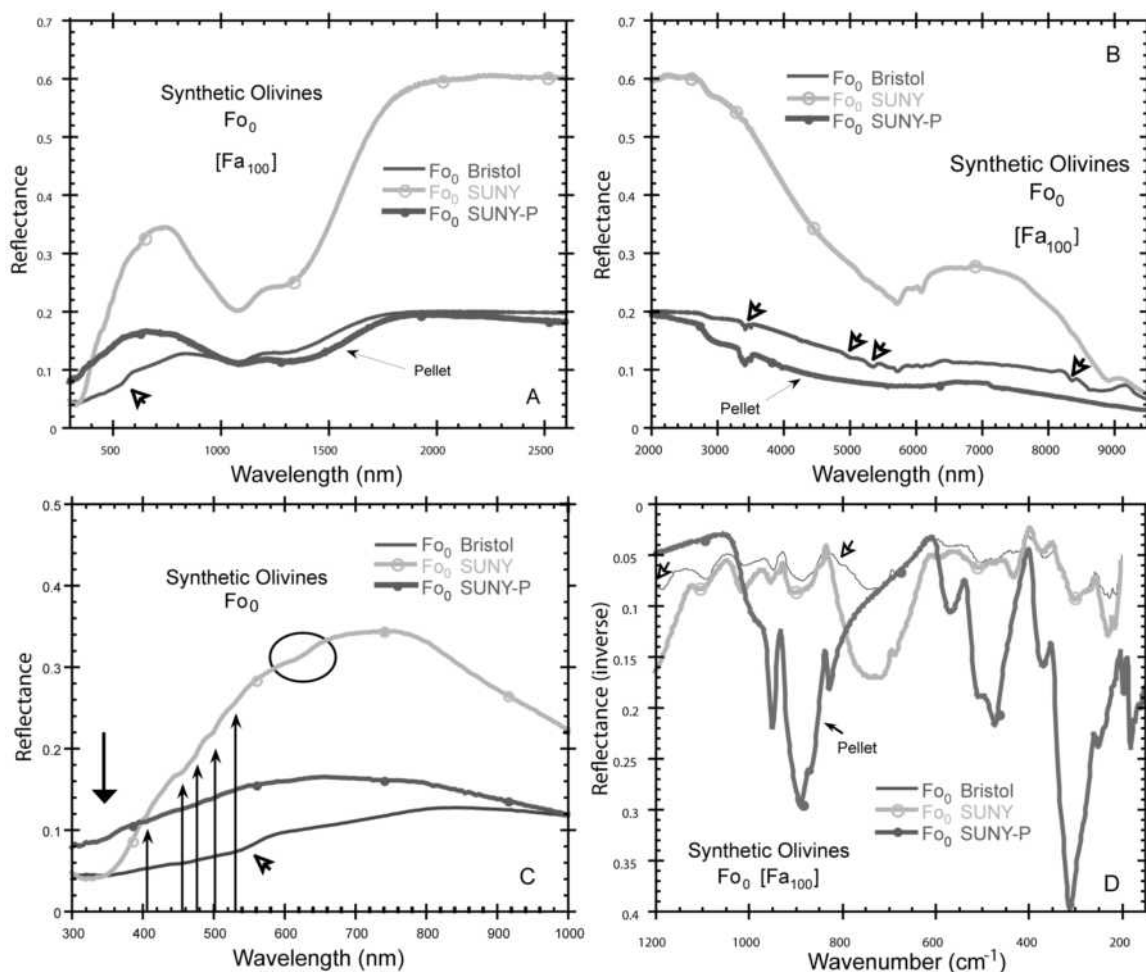


FIGURE 8. Reflectance spectra for Fo_0 samples acquired in the RELAB. Fo_0 Bristol and SUNY are fine-grained powders. Fo_0 SUNY-P is the pressed pellet made from Fo_0 SUNY. All features are characteristic of olivine except those indicated with an open arrow due to contaminants present (see text). (a) VNIR bidirectional reflectance spectra. Features arise from radiation transmitted through particles (the body component). (b) Extended near-infrared reflectance spectra acquired in a purged environment (off-axis biconical geometry). Features arise from the body component. (c) Expanded bidirectional reflectance spectra across the visible with spin-forbidden transitions indicated with small arrows. Metal-oxygen charge transfer is indicated with a large arrow. (d) Mid-infrared reflectance spectra acquired in a purged environment (off-axis biconical geometry). Features arise largely from interaction with the surface of particles. The scale is inverted for ease of comparison with emissivity spectra (see Fig. 11). The two powder samples exhibit additional “Transparency Features” (Salisbury 1993) that are prominent in the 950–600 cm^{-1} region where k is low.

between 2000 and 9000 nm. This is typically called “volume scattering” because radiation passes through many grains before being scattered out of the sample. Prominent olivine absorption features, caused by overtones of vibrations of SiO_4 tetrahedra, are evident near 5500 nm in the Fo_0 SUNY spectrum of Figure 8b. Due to the compressed form of the pellet sample, however, the spectrum of the Fo_0 SUNY-pellet remains dark also across these wavelengths because little radiation is allowed to scatter out of the sample. These olivine overtone absorptions are weakly discernable in the spectrum of the Fo_0 Bristol sample. Some organic contamination is present in both the Fo_0 Bristol sample and the Fo_0 SUNY pellet, as evidenced by sharp features near 3200 nm (open arrow in Fig. 8b).

The VNIR wavelength spectra of the synthetic fayalites (Fig. 8c) are dominated by the edge of a strong Fe^{2+} -O charge transfer band. Superimposed on the limb of the metal-oxygen charge transfer absorption are a series of weak bands caused by spin-

forbidden transitions of Fe^{2+} in the M1 and M2 cation sites, the most distinctive of which are highlighted in Figure 8c by small vertical arrows. These features are similar to, but slightly weaker than the spin-forbidden features that occur in pyroxenes, the most prominent and well-studied of which occurs near 506 nm (e.g., Burns et al. 1972; Hazen et al. 1978; Goldman and Rossman 1979; Klima et al. 2007). An additional weak feature is present near 610 nm in the fayalite spectrum. This feature, circled in Figure 8c, is broader than the spin-forbidden absorption bands, and it occurs at a significantly lower energy (longer wavelength) than predicted for any spin-forbidden transitions in olivine. At this time we cannot assign a cause to this band.

In contrast to the VNIR, where light needs to penetrate into a crystal to produce absorption bands, features in the mid- and far-infrared are discerned when radiation interacts with the surface of a particle (“surface scattering”) (e.g., Salisbury 1993). At mid-infrared wavelengths, intense absorptions are caused

by fundamental vibrations of the silica tetrahedra (described in more detail below in the thermal emission spectroscopy section). With little to no multiple scattering at the sample surface (nor penetration into the grains for volume scattering), the spectrum of the Fo_0 SUNY-pellet exhibits the strongest olivine features at these wavelengths (Fig. 8d). Although multiple/volume scattering effects are present for spectra of the fine-grained particulate samples, absorptions caused by fundamental vibrations of the silica tetrahedra are seen clearly for SUNY Fo_0 and even for Bristol Fo_0 .

At all visible and near-infrared wavelengths, the Fo_0 SUNY sample exhibits absorption bands that are diagnostic of a pure Fe^{2+} olivine. Though the Fo_0 Bristol sample is also dominated by fayalite, the contamination present makes it unsuitable for characterizing the spectral parameters for a pure Fe^{2+} end-member olivine.

VNIR spectral modeling

The Modified Gaussian Model (MGM) was used to provide a quantitative analysis of the diagnostic crystal field absorptions near 1000 nm of pure fayalite for the powdered Fo_0 SUNY sample. The results of the final model run are presented in Figure 9. Data are plotted in natural log reflectance, as it provides an approximation for absorbance.

Absorption bands in the VNIR spectrum of Fo_0 SUNY can be grouped into three categories: spin-allowed crystal field transitions, oxygen-metal charge transfer, and spin-forbidden crystal field transitions. The three spin-allowed crystal field absorption bands are shown in black in Figure 9. The first and third, centered at 906 and 1283 nm, respectively, are assigned to transitions of Fe^{2+} in the M1 site of olivine. The middle band, centered at 1074 nm, is caused by Fe^{2+} in the M2 site. These band positions are consistent with those derived by Sunshine and Pieters (1998) for a suite of natural olivines, as illustrated in Figure 10. Specifically, the Fo_0 SUNY sample (represented by black diamonds in Fig. 10) exhibits crystal field bands at almost the exact same wavelengths as the natural Rockport fayalite (R).

Oxygen-metal charge transfers are generally centered in the

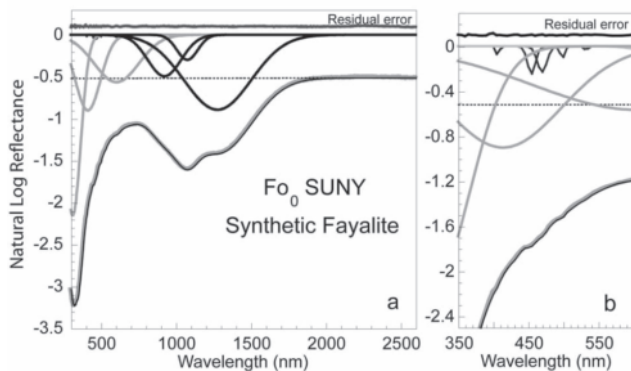


FIGURE 9. MGM deconvolution of the Fo_0 SUNY powdered synthetic fayalite sample. The spectrum of the sample is shown in gray with the model fit superimposed as a thin black line. The continuum is indicated by a dashed line, and deconvolved bands are shown at the top. The residual error as a function of wavelength is also presented. The full deconvolution is shown in **a**, while **b** is a 5 \times enlargement to show the spin-forbidden bands.

UV, but move to longer wavelengths with increasing iron content. The MGM was developed to model spin-allowed crystal field absorption bands, and thus, the modified Gaussian curve may not be ideal to model charge transfer bands. Nonetheless, we used three modified Gaussian curves, shown in dark gray in Figure 9, to model the Fe^{2+} -O charge transfer. The center of the strongest of these bands, modeled at 322 nm, is the most significant parameter in that it does not depend strongly on the shape of the charge transfer energy distribution or the input model parameters. The centers and widths of the additional “charge transfer” bands vary based on the starting conditions of the model, and may either describe the tail of the strong band or an additional absorption.

Using the crystal field splitting for olivine M1 and M2 sites from Burns (1993) and a Racah B parameter of 1058 cm^{-1} for Fe^{2+} from Cotton (1963) with a Tanabe-Sugano diagram for a d^6 cation in an octahedral crystal field, the positions of spin-forbidden transitions can be predicted. The lowest energy spin-forbidden transition is predicted to occur near 530 nm, followed by nine additional transitions between roughly 505 and 310 nm. Five of these are visually evident in the spectrum of Fo_0 SUNY and the RMS error of the general 6-band fit and have thus been included as bands in the final MGM fit (Fig. 9). These features, though orders of magnitude weaker than the spin-allowed crystal field bands, are consistently observed throughout the synthetic olivines.

Thermal emission and specular reflectance spectroscopy

The relationship between the structure and chemistry of olivine and its fundamental spectral vibrations has been described by Duke and Stephens (1964) and Tarte (1963). The mid-infrared emissivity (ϵ) spectrum of the Fo_0 SUNY pellet sample, as compared to the two mid-infrared reflectance (R) measurements of this sample, is shown in Figure 11. The emissivity values below 240 cm^{-1} are not shown due to noise

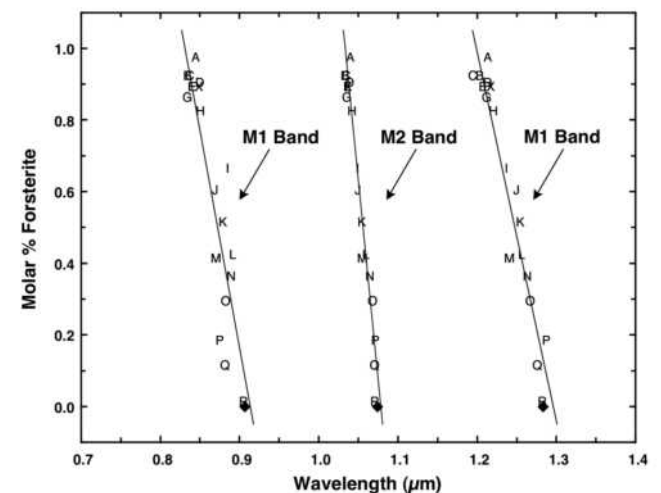


FIGURE 10. Band positions of spin-allowed crystal field bands for synthetic fayalite Fo_0 SUNY (solid diamonds at 0.0 on the y axis) compared with natural olivines (A to R) as analyzed by Sunshine and Pieters (1998). The synthetic sample (black diamond at 0.0 on the y axis) falls on the composition trends defined by natural samples and is indistinguishable from the natural Fo_{01} fayalite, R, from Rockport, Massachusetts.

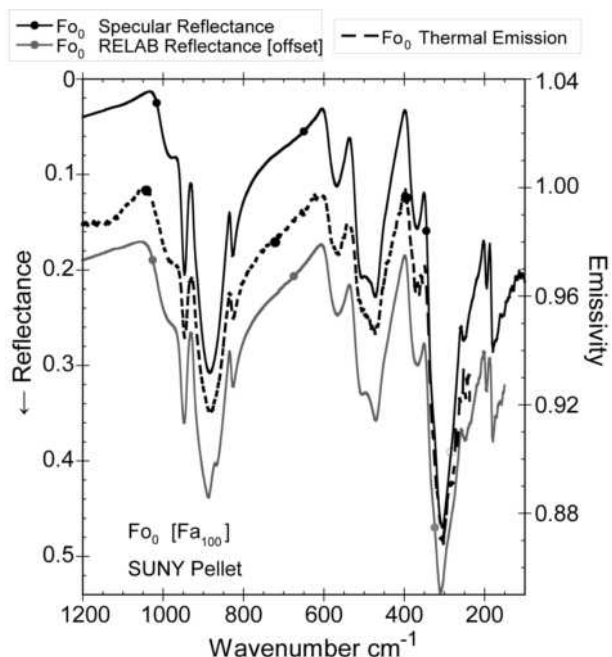


FIGURE 11. Thermal emission spectrum of Fo_0 pellet compared with specular and diffuse reflectance spectra of the same sample. Reflectance spectra are inverted for comparison to the emission spectrum (and are related through Kirchhoff's Law where $\epsilon = 1 - R$). Spectra are offset for clarity.

from atmospheric contaminants. The ϵ and R data are related according to Kirchhoff's Law, which states that $\epsilon = 1 - R$, and the reflectance spectra are broadly similar to the inverse of the emissivity spectrum as expected. Mid-IR band assignments for olivine were first presented for transmittance spectra, where the allowed transitions include ν_1 near 830 cm^{-1} , ν_2 near 370 cm^{-1} , a ν_3 triplet between 825 and 1000 cm^{-1} , and a ν_4 triplet between 460 and 610 cm^{-1} (Duke and Stephens 1964; Tarte 1963). The band positions and shapes are shifted slightly for reflectance and emittance spectra because both the real and imaginary optical constants contribute to the latter.

The emissivity and reflectance spectra in Figure 11 exhibit multiple clearly discernable olivine bands in this spectral region. Eight emissivity bands are observed whose minima occur at 979 , 946 , 886 , 826 , 565 , 472 , 363 , and 304 cm^{-1} . There is an additional shoulder that occurs at $\sim 505\text{ cm}^{-1}$, but it is fairly indistinct (albeit more distinct in the two reflectance spectra). Bands are present at 978 , 947 , 885 , 826 , 568 , 510 , 472 , 368 , 304 , 250 , 195 , 179 , and 155 cm^{-1} in the specular reflectance spectrum and at nearly identical positions in the biconical RELAB reflectance spectrum.

The first three emissivity bands at 979 , 946 , and 886 cm^{-1} result from the asymmetric Si-O stretching vibrations (ν_3). The band at 826 cm^{-1} is due to the symmetric stretching vibration (ν_1) and the longer-wavelength bands at 565 and 472 plus the shoulder at $\sim 505\text{ cm}^{-1}$ result from the ν_4 bending modes. The remaining bands are due to translations of the SiO_4 tetrahedra and translations of the Fe in the structure (Bowey et al. 2001) as are the low-wavenumber bands not available in the emissivity data (Hofmeister 1986, 1997; Fabian et al. 2001).

As mentioned earlier, octahedral cations fill M1 and M2 sites where the M1 octahedron shares two edges with a SiO_4

tetrahedron and the M2 octahedron shares one edge with a SiO_4 tetrahedron. This edge-sharing is the principle factor causing distortion of the Td symmetry of the SiO_4 groups (Farmer 1974). The Mg^{2+} cation is much smaller than the Fe^{2+} cation and for this reason Mg^{2+} disrupts the Td structure to a greater extent. Olivine absorption spectra exhibit shifts toward higher frequencies (shorter wavelengths) for Mg compared to larger cations (Burns and Huggins 1972; Tarte 1963, 1965). The fayalite bands shown in Figure 11 are all offset to lower frequency (smaller wavenumbers) than corresponding emissivity bands for a pure forsterite (not shown, data from M. Lane, unpublished data). Previous works (e.g., Tarte 1963; Duke and Stephens 1964; Burns and Huggins 1972; Farmer 1974; Jeanloz 1980; Reynard 1991; Salisbury et al. 1991; Hofmeister 1997; Koepfen and Hamilton 2008) show this relationship as well for the Fe-Mg olivine minerals.

Attenuated total reflectance

The ATR spectrum of the Fo_0 SUNY sample is shown in Figure 12. ATR spectra were collected from 250 – 4000 cm^{-1} . Band positions in the ATR spectrum are all at lower wavenumbers (longer wavelengths) than those of the reflectance and emissivity spectra shown in Figure 11. This is due to the fact that an ATR absorbance spectrum relies only on its absorption coefficient, while a reflectance or emissivity spectrum is a function of k and n , the real part of the complex index of refraction (Piro et al. 1988). Band positions in the ATR spectrum are 943 , 856 , 825 , 560 , 465 , 363 , and 226 cm^{-1} . Weak shoulders are present at 965 , 912 , 498 , and 325 cm^{-1} .

Because olivine is not an isotropic mineral, infrared spectra vary depending on the crystal axis measured (e.g., Hofmeister 1986, 1997; Fabian et al. 2001; Suto et al. 2002). The fayalite sample measured in this study is a synthetic sample that was ground into a fine powder for synthesis and later pressed into a compact pellet for specular reflectance measurements. There-

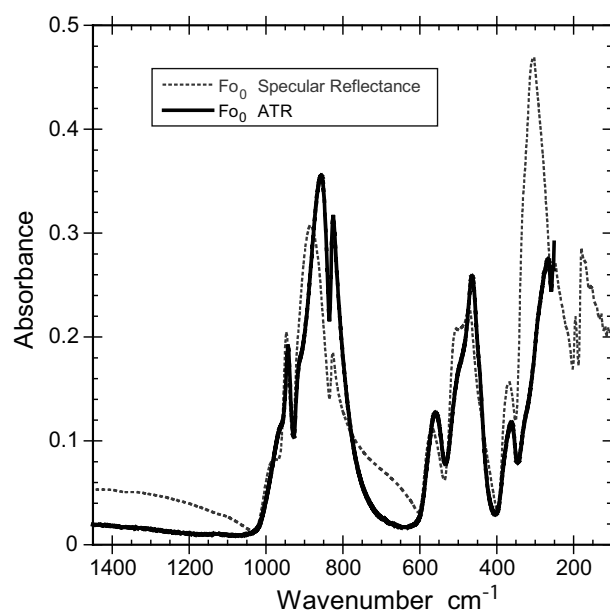


FIGURE 12. Attenuated total reflectance (ATR) spectrum combined with specular reflectance of Fo_0 SUNY.

fore, both the ATR and specular reflectance (as well as thermal emissivity) spectra are due to a combination of many crystal orientations.

Optical constants

We calculated the optical constants of the Fo₀ SUNY sample using the methods of Glotch et al. (2007). We used 22 oscillators and an ϵ_0 value of 3.9843 to model the SUNY Fo spectrum. The oscillator parameters are shown in Table 4, and the measured and modeled spectra and the real (n) and imaginary (k) refractive indices are shown in Figure 13. The ϵ_0 value of 3.9843 is only slightly higher than the theoretical value of ~ 3.46 based on the square of the visible index. This could be due to the fact that only a portion (100–2000 cm⁻¹) of the full fayalite spectral range is modeled. The measured and modeled spectra, as well as the modeled real and imaginary refractive indices are available at the Stony Brook University Optical Constant Database at http://ms.cc.sunysb.edu/~tglotch/optical_constants.htm.

ADVANTAGES OF THE INTEGRATED SPECTROSCOPIC APPROACH

Mars exploration is largely dependent on remote sensing and in situ data for understanding the character and evolution of the surface. Interpretation of remote sensing and in situ data in turn depend on accurate laboratory data with solid theoretical understanding. Relations between results from different techniques, however, are often not easily integrated. Each technique has its own theoretical basis and database using laboratory measurements of materials, but the samples in those databases rarely cross over from one technique to the other. Conclusions about compositional properties, for example, are very dependent on the specific technique used. Fortunately, as the orbital and in situ elements of the Mars Exploration Program continue to be implemented, multiple types of sensors for mineralogical analyses (VNIR, thermal infrared, Mössbauer) enable the uncertainty to be decreased by providing multiple tests for mineral assessment. Because very little cross-calibrated data exist that can be used

across multiple sensors, we intend to close that gap with carefully planned consortium analyses that produce a full range of spectroscopic data and related detailed information that are the best possible analogs for analyses of terrestrial planetary surfaces. The results presented here for Fo₀ are only the beginning of that effort, and work is already in progress to report on specifics of thermal emission and attenuated total reflectance, diffuse and specular reflectance (Lane et al. in preparation), VNIR (Pieters et al. in preparation), and Mössbauer spectroscopy (Dyar et al. in preparation) of the entire Fe²⁺-Mg suite of these samples.

In this study, Mössbauer data are used for two purposes: to test for the presence of impurities resulting from synthesis, and to ensure that the samples studied are indeed the pure synthetic compositions desired. Although all but two of the Bristol samples in the suite (Fo₄₀ and Fo₅₀) failed this test (Table 1), some of the impure samples will nonetheless have future usefulness because their spectra can be used to model slightly oxidized olivines, and those models will be constrained by quantitative knowledge of how much Fe³⁺ is present. On the other hand, Mössbauer data show that the SUNY suite of synthetic olivines is free of Fe³⁺ and impurities at the >1% level, so these are identified as the best samples for further integrated analyses. Calculations of recoil-free fractions for the M1 and M2 sites in olivine were unfortunately not possible, but an overall idea of f values for the mixed doublet is now known.

The other types of spectroscopy used in this study are also sensitive, to varying degrees, to the different types of contamination in Fo₀. Raman, for example, identified the presence of hematite caused by oxidation from its laser; it is unfortunate that the resultant alteration made it challenging to relate the Raman spectra to the other spectroscopic techniques for pure fayalite. However, the fact that small amounts of Mg mitigates such oxidation should allow Raman to play a complementary role in the wider study of samples with Fo > 0. Diffuse reflectance measurements (VNIR) showed an additional feature from a contaminating phase (consistent with hematite) that is present near 550 nm for the Fo₀ Bristol sample, as well as minor organic contamination

TABLE 4. Oscillator parameters for the SUNY Fo₀ spectrum

ν (cm ⁻¹)	γ	$4\pi\rho$
180	0.0540	0.6859
197	0.0284	0.1628
250	0.0691	0.5123
279	0.0485	1.3780
288	0.0453	1.3915
297	0.0452	0.8117
328	0.0448	0.0348
359	0.0764	0.2189
375	0.0605	0.0857
467	0.0607	0.5492
487	0.0518	0.1006
502	0.0465	0.1008
512	0.0521	0.0505
554	0.0463	0.0816
568	0.0391	0.0528
582	0.0357	0.0245
811	0.0485	0.0660
826	0.0117	0.0709
859	0.0370	0.6207
901	0.0513	0.0403
939	0.0134	0.0299
979	0.0484	0.0377

Note: $\epsilon_0 = 3.9843$.

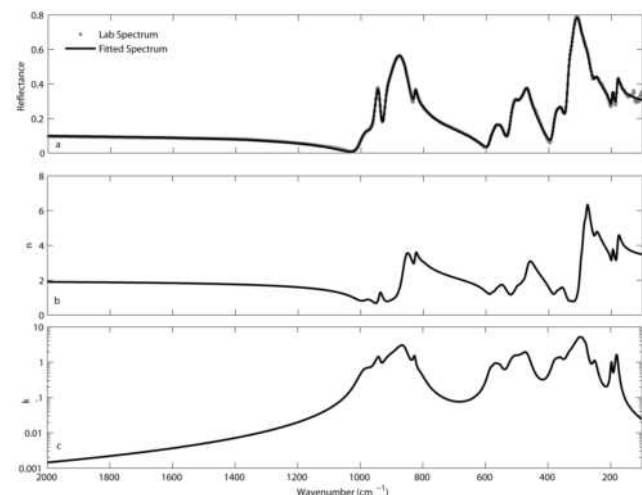


FIGURE 13. Optical constants derived from the SUNY Fo₀ pellet. All spectra cover the spectral range 100–2000 cm⁻¹. (a) Measured and modeled spectra. (b) Real index of refraction (n). (c) Imaginary index of refraction (k).

in both the Fo₀ Bristol sample and the Fo₀ SUNY pellet (sharp features near 3200 nm). The presence of hematite inferred from the Bristol Fo₀ reflectance measurements is consistent with, though not proven by, the Mössbauer data that are suggestive of nanophase oxide. However, the Mössbauer data constrain the abundance of iron oxide in the bulk sample (measured by Mössbauer and thermal emission) to be very small.

In contrast to the preceding techniques, in which energy (light) needs to penetrate into a crystal to produce absorption bands, features in the mid- and far-infrared are generally dominated by interactions of radiation with the surface of a particle. Thus, these methods will be more sensitive to surface issues (and impurities such as coatings). In these synthetic olivines (as noted in the olivine synthesis section), incompletely reacted olivines usually had impurities in their cores. Because they “see” only grain surface interactions, mid- and far-infrared reflectance techniques would not be expected to detect those contaminating phases in the interiors of mineral grains. Thermal emission measurements are generally thought to detect to depths down to ~50 μm, though they have been shown to be sensitive to rock coatings as little as ~6 μm thick (Minitti et al. 2007). Depending on the grain-size distribution of the sample and the sizes of the grains, the thermal emissivity spectra might be representative of both the grain surfaces and the cores in an intimate mixture.

Finally, it is worth mentioning that particle size and texture are important for the VNIR methods, but are unimportant for Mössbauer and Raman, which use randomly oriented thin absorbers and single crystals, respectively. It is clear that different techniques provide complementary types of information, and that there is much to be learned by the combination of analytical methods employed herein. VNIR and mid-infrared (MIR) reflectance and emission measurements are most directly comparable to remote sensing measurements made of Mars and other bodies. Shifts seen in visible absorption may indicate the presence of minor cation substitution. ATR spectroscopy is most sensitive to mineral surfaces and can detect surface bound water if present. Along with VNIR spectroscopy, it is also better suited to analysis of fine particulates than MIR reflectance or emission spectroscopy.

In short, each spectroscopic technique provides valuable, and in some cases unique, characterization of planetary materials. With this example of different suites of synthetic olivines, regular features are observed as the composition and structure vary that are understood from mineral physics principles. Minor contaminants can play a strong or a weak role on the observations and are critical to document. As illustrated with an unusual Mars dunite (Pieters et al. 2008), it is often only through the use of multiple techniques to examine a previously unknown material that simple ambiguities or profound mysteries can be resolved.

ACKNOWLEDGMENTS

We thank Mickey Gunter for help with Figure 1, and Phil Christensen at Arizona State University for the use of his thermal emission spectrometer facility. This manuscript was greatly improved by the careful work of Associate Editor Rhian Jones, and thorough reviews from David Agresti and William Koeppen, for which we are very grateful. This work was supported by NSF grant EAR-0439161 and NASA grants NNG04GG12G (M.D.D.), NNG06G130G (M.D.D.), NNX07AR66G (C.M.P., J.L.B., M.D.D., T.H., M.D.L., J.S.). RELAB is operated as an open multi-user facility under grant NNG06GJ31G. O.N.M. and P.A.B. would like to acknowledge the support of the Royal Society and the PPARC/STFC under grant PPA/G/S/2003/00071. This is PSI publication 456.

REFERENCES CITED

- Aikawa, N., Kumazawa, M., and Tokonami, M. (1985) Temperature dependence of intersite distribution of Mg and Fe in olivine and the associated change of lattice-parameters. *Physics and Chemistry of Minerals*, 12, 1–8.
- Akamatsu, T., Kumazawa, M., Aikawa, N., and Takei, H. (1993) Pressure effect on the divalent cation distribution in nonideal solid solution of forsterite and fayalite. *Physics and Chemistry of Minerals*, 19, 423–444.
- Bancroft, G.M. (1969) Quantitative site populations in silicate minerals by the Mössbauer effect. *Chemical Geology*, 5, 255–258.
- Bish, D.L. (1981) Cation ordering in synthetic and natural Ni-Mg olivine. *American Mineralogist*, 66, 770–776.
- Bowey, J.E., Lee, C., Tucker, C., Hofmeister, A.M., Ade, P.A.R., and Barlow, M.J. (2001) Temperature effects on the 15–85 mm spectra of olivines and pyroxenes. *Monthly Notices of the Royal Astronomical Society*, 325, 886–896.
- Burns, R.G. (1970) Crystal field spectra and evidence for cation ordering in olivine minerals. *American Mineralogist*, 55, 1608–1632.
- (1993) *Mineralogical Applications of Crystal Field Theory*, 551 p. Cambridge University Press, U.K.
- Burns, R.G. and Huggins, F.E. (1972) Cation determinative curves for Mg-Fe-Mn olivines from vibrational spectra. *American Mineralogist*, 57, 967–985.
- Burns, R.G., Huggins, F.E., and Abu-Eid, R.M. (1972) Polarized absorption spectra of single crystals of lunar pyroxenes and olivines. *Earth, Moon, and Planets*, 4, 93–102.
- Chopelas, A. (1991) Single crystal Raman spectra of forsterite, fayalite, and monticellite. *American Mineralogist*, 76, 1101–1109.
- Cotton, F.A. (1963) *Chemical Applications of Group Theory*, 295 p. Wiley, New York.
- de Faria, D.L.A., Venâncio Silva, S., and de Oliveira, M.T. (2007) Raman microspectroscopy of some iron oxides and oxyhydroxides. *Journal of Raman Spectroscopy*, 28, 873–878.
- DeGrave, E. and VanAlboom, A. (1991) Evaluation of ferrous and ferric Mössbauer fractions. *Physics and Chemistry of Minerals*, 18, 337–342.
- DeGrave, E., Verbeeck, A.E., and Chambaere, D.G. (1985) Influence of small aluminum substitutions on the hematite lattice. *Physics Letters*, 107A, 181–184.
- Duke, D.A. and Stephens, J.D. (1964) Infrared investigation of the olivine group minerals. *American Mineralogist*, 49, 1388–1406.
- Dyar, M.D., Schaefer, M.W., Sklute, E.C., and Bishop, J.L. (2008) Mössbauer spectroscopy of phyllosilicates: Effects of fitting models on recoil-free fractions and redox ratios. *Clay Minerals*, 43, 3–33.
- Eeckhout, S.G. and DeGrave, E. (2003) Evaluation of ferrous and ferric Mössbauer fractions. Part II. *Physics and Chemistry of Minerals*, 30, 142–146.
- Fabian, D., Henning, T., Jäger, C., Mutschke, H., Dorschner, J., and Wehrhan, O. (2001) Steps toward interstellar silicate mineralogy VI. Dependence of crystalline olivine IR spectra on iron content and particle shape. *Astronomy and Astrophysics*, 378, 228–238.
- Farmer, V.C. (1974) Orthosilicates, pyrosilicates, and other finite-chain silicates. In V.C. Farmer, Ed., *The Infrared Spectra of Minerals*, p. 285–303. The Mineralogical Society, London.
- Glotch, T.D., Morris, R.V., Christensen, P.R., and Sharp, T.G. (2004) Effect of precursor mineralogy on the thermal infrared emission spectra of hematite: Application to Martian hematite mineralization. *Journal of Geophysical Research*, 109, E07003, DOI: 10.1029/2003JE002224.
- Glotch, T.D., Rossman, G.R., and Aharonson, O. (2007) Mid-infrared (5–100 μm) infrared reflectance spectra and optical constants of ten phyllosilicate minerals. *Icarus*, 192, 605–622.
- Goldman, D.S. and Rossman, G.R. (1979) Determination of quantitative cation distribution in orthopyroxenes from electronic absorption spectra. *Physics and Chemistry of Minerals*, 4, 43–53.
- Hazen, R.M., Bell, P.M., and Mao, H.K. (1978) Effects of compositional variation on absorption spectra of lunar pyroxenes. *Proceedings of the Ninth Lunar and Planetary Science Conference*, 3, p. 2919–2934. Pergamon Press, New York.
- Henderson, C.M.B., Knight, K.S., Redfern, S.A., and Wood, B.J. (1996) High-temperature study of octahedral cation exchange in olivine by neutron powder diffraction. *Science*, 271, 1713–1715.
- Hofmeister, A.M. (1986) Single-crystal absorption and reflection infrared spectroscopy of forsterite and fayalite. *Physics and Chemistry of Minerals*, 14, 499–513.
- (1997) Infrared reflectance spectra of fayalite, and adsorption data from assorted olivines, including pressure, and isotope effects. *Physics and Chemistry of Minerals*, 24, 535–546.
- Hu, N., Langer, K., and Boström, K. (1990) Polarized electronic absorption spectra and Ni-Mg partitioning in olivines (Mg_{1-x}Ni_x)₂[SiO₄]. *European Journal of Mineralogy*, 2, 29–41.
- Jeanloz, R. (1980) Infrared spectra of olivine polymorphs: α, β phase and spinel. *Physics and Chemistry of Minerals*, 5, 327–341.
- Klima, R.A., Dyar, M.D., and Pieters, C.M. (2007) Spectroscopy of synthetic Mg-Fe pyroxenes I: Spin-allowed and spin-forbidden crystal field bands in the visible

- and near-infrared. *Meteoritics and Planetary Science*, 42, 235–254.
- Koeppen, W.C. and Hamilton, V.E. (2008) Global distribution, composition, and abundance of olivine on the surface of Mars from thermal infrared data. *Journal of Geophysical Research*, 113, E05001, DOI: 10.1029/2007JE002984.
- Kuebler, K.E., Jolliff, B.L., Wang, A., and Haskin, L.A. (2006) Extracting olivine (Fo–Fa) compositions from Raman spectral peak positions. *Geochimica et Cosmochimica Acta*, 70, 6201–6222.
- Lafleur, L.D. and Goodman C. (1971) Characteristic temperatures of the Mössbauer fraction and thermal-shift measurements in iron and iron salts. *Physics Reviews B*, 4, 2915–2920.
- Martin, T.P., Merlin, R., Huffman, D.R., and Cardona, M. (1977) Resonant two magnon Raman scattering in α -Fe₂O₃. *Solid State Communications*, 22, 565–567.
- Menzies, O.N., Bland, P.A., and Berry, F.J. (2001) An ⁵⁷Fe Mössbauer study of the olivine solid solution series: Implications for meteorite classification and deconvolution of unequilibrated chondrite spectra. 32nd Annual Lunar and Planetary Science Conference, Houston, Texas, Abstract 1622.
- Minitti, M.E., Weitz, C.M., Lane, M.D., and Bishop, J.L. (2007) Morphology, chemistry, and spectral properties of Hawaiian rock coatings and implications for Mars. *Journal of Geophysical Research*, 112, E05015, DOI: 10.1029/2006JE002839.
- Ottonello, G., Della Giusta, A., and Molin, G.M. (1990) Cation ordering in Ni-Mg olivines. *American Mineralogist*, 74, 411–421.
- Pieters, C.M., Klima, R.L., Hiroi, T., Dyar, M.D., Lane, M.D., Treiman, A.H., Noble, S.K., Sunshine, J.M., and Bishop, J.L. (2008) Martian dunite NWA 2737: Integrated spectroscopic analyses of brown olivine. *Journal of Geophysical Research*, 113, E06004, DOI: 10.1029/2007JE002939.
- Piro, O.E., Castellano, E.E., and Gonzalez, S.R. (1988) Attenuated total-reflectance of strongly absorbing anisotropic single crystals: Trigonal α -quartz. *Physics Reviews B*, 38, 8437–8443.
- Redfern, S.A.T., Artioli, G., Rinaldi, R., Henderson, C.M.B., Knight, K.S., and Wood, B.J. (2000) Octahedral cation ordering in olivine at high temperature. II: an in situ neutron powder diffraction study on synthetic MgFeSiO₄ (Fa50). *Physics and Chemistry of Minerals*, 27, 630–637.
- Reynard, B. (1991) Single-crystal infrared reflectivity of pure Mg₂SiO₃ forsterite and (Mg_{0.86},Fe_{0.14})₂SiO₄ olivine. *Physics and Chemistry of Minerals*, 18, 19–25.
- Roush, T., Pollack, J., and Orenberg, J. (1991) Derivation of midinfrared (5–25 μ m) optical constants of some silicates and palagonite. *Icarus*, 94, 191–208.
- Ruff, S.W., Christensen, P.R., Barbiera, P.W., and Anderson, D.L. (1997) Quantitative thermal emission spectroscopy of minerals: A laboratory technique for measurement and calibration. *Journal of Geophysical Research B*, 102, 14899–14913.
- Salisbury, J.W. (1993) Mid-infrared spectroscopy: Laboratory data. In C.M. Pieters and P.A.J. Englert, Eds., *Remote Geochemical Analysis: Elemental and Mineralogical Composition*, p. 79–98. Cambridge University Press, New York.
- Salisbury, J.W., Walter, L.S., Vergo, N., and D’Aria, D.M. (1991) Infrared (2.1–25 micrometers) Spectra of Minerals, 294 p. The Johns Hopkins University Press, Baltimore.
- Sklute, E.C., Dyar, M.D., and Schaefer, M.W. (2006) Mössbauer spectroscopy of olivines across the Mg-Fe solid solution. 37th Annual Lunar and Planetary Science Conference, League City, Texas, Abstract 2109.
- Spitzer, W.G. and Kleinman, D.A. (1961) Infrared lattice bands of quartz. *Physical Reviews*, 121, 1324–1335.
- Sunshine, J.M. and Pieters, C.M. (1998) Determining the composition of olivine from reflectance spectroscopy. *Journal of Geophysical Research*, 103, 13675–13688.
- Sunshine, J.M., Pieters, C.M., and Pratt, S.F. (1990) Deconvolution of mineral absorption bands: An improved approach. *Journal of Geophysical Research*, 95, 6955–6966.
- Sunshine, J.M., Bus, S.J., Corrigan, C.M., McCoy, T.J., and Burbine, T.H. (2007) Olivine-dominated asteroids and meteorites: Distinguishing nebular and igneous histories. *Meteoritics and Planetary Science*, 42, 155–170.
- Suto, H., Koike, C., Sogawa, H., Tsuchiyama, A., Chihara, H., and Mizutani, K. (2002) Infrared spectra of fayalite crystal. *Astronomy and Astrophysics*, 389, 586–571.
- Tarte, P. (1963) Etude infra-rouge des orthosilicates et des orthogermanates. *Spectrochimica Acta*, 19, 25–47.
- (1965) Experimental study and interpretation of infrared spectra of silicates and germanates. *Mémoires de la Classe des Sciences. Académie Royale de Belgique. Collection*, 35, 4a–b, 58–81.
- Teichgraber, C. and Freund, F. (2008) Polarizability of Si-O bonds in olivine as a function of temperature: A Raman study. *Eos, Transactions of the American Geophysical Union, Fall Meeting*, Abstract MR53A-1726.

MANUSCRIPT RECEIVED OCTOBER 11, 2008

MANUSCRIPT ACCEPTED MARCH 17, 2009

MANUSCRIPT HANDLED BY RHIAN JONES